Simulation of the El Niño Southern Oscillation: Results from the Coupled Model Intercomparison Project

Krishna AchutaRao[1], Kenneth R. Sperber[1],
and the CMIP Modelling Groups[2-14]

[1]Program For Climate Model Diagnosis and Intercomparison, Lawrence Livermore National Laboratory, Livermore, CA USA

[2]Bureau of Meteorology Research Centre, Melbourne, Australia

[3]Canadian Centre for Climate Modelling and Analysis, Victoria, Canada

[4]Center for Climate System Research, Tokyo, Japan

[5]Centre Européen de Recherche et de Formation Avancée en Calcul Scientifique, Toulouse, France

[6]Commonwealth Scientific & Industrial Research Organization, Mordialloc, Australia

[7]Geophysical Fluid Dynamics Laboratory, Princeton, NJ USA

[8]Institute of Atmospheric Physics, Beijing, China

[9]Laboratorie de Météorologie Dynamique, Paris, France

[10]Max-Planck-Institut für Meteorologie, Hamburg, Germany

[11]Meteorological Research Institute, Tsukuba, Japan

[12]NASA Goddard Institute for Space Studies, New York, NY USA

[13]National Center for Atmospheric Research, Boulder, CO, USA

[14]United Kingdom Meteorological Office, Bracknell, United Kingdom

Corresponding Author:
Dr. Krishna AchutaRao
Program for Climate Model Diagnosis and Intercomparison
Lawrence Livermore National Laboratory
P.O. Box 808, L-264
Livermore, CA 94550 USA

Ph: (925) 422-4197
Fax: (925) 422-7675
Email: achutarao1@llnl.gov

Abstract

The El Niño Southern Oscillation (ENSO) simulations of 17 global coupled ocean-atmosphere general circulation models (CGCMs) from the Coupled Model Intercomparison Project (CMIP) are analyzed. Monthly mean values of surface air temperature, sea level pressure and precipitation for 80 years are analyzed from control runs. Nearly half of the models studied do not employ any form of flux correction. Flux-corrected CGCMs were better at simulating the base state and annual cycle of the temperature field in the equatorial Pacific but not necessarily better at simulating ENSO variability. While a subset of the models produce realistic amplitudes of NIÑO3 and the Southern Oscillation Index (SOI), ENSO often tends to occur at a higher than observed frequency. A few models also capture the teleconnection between NIÑO3 temperature anomalies, SOI, and the global surface air temperature, sea level pressure and precipitation. Only a few models simulate phase locking of ENSO with the seasonal cycle. Most models have problems in simulating the ENSO related sea-level pressure variations over the eastern Pacific and this is associated with errors in the precipitation response. The models fall into 3 distinct categories based on their ability to simulate large-scale ENSO related patterns of sea-level pressure, surface air temperature and precipitation. Group 1 consists of models that represent well the Walker circulation anomalies, the warming and enhanced rainfall in the central/east Pacific. Models in Group 2 exhibit a westward displacement and/or have weak responses, while Group 3 models have the weakest ENSO signatures.

1. Introduction

The El Niño Southern Oscillation (ENSO) - a phenomenon driven by coupled processes is one of the most important sources of interannual variability in the natural climate system (Philander (1990)). El Niño events, characterized by increased sea surface temperatures in the central and eastern tropical Pacific, have a periodicity of between two and seven years. The early 1990s, characterized by prolonged El Niño conditions, and the strong event of 1997-98 (see McPhaden (1999)) have been unusual compared with past ENSO variability. The extended duration and apparent increase in the frequency of these events have further heightened interest in studying ENSO. The apparent climate shift in the tropical Pacific around 1976 (Trenberth (1990), Nicholls et al. (1996), Trenberth and Hoar (1996, 1997)) was preceded by a period of reduced variability between 1920-1960 indicating an interdecadal modulation of ENSO.

The effects of ENSO events are felt outside of the tropical Pacific Ocean (Trenberth et al. (1998), Rasmusson and Carpenter (1982), Bradley et al. (1987), Ropelewski and Halpert (1987, 1989)) including a modulation of temperatures globally (Jones (1988), Angell (1990, 2000), Boden et al. (1990, 1992), Privalsky and Jensen (1995), Wigley (2000)). Transient CO_2 CGCM experiments (e.g., Meehl et al. (1993), Knutson and Manabe (1994, 1995), Tett (1995) and Timmermann et al.(1999)) have raised some concerns over the possible changes in ENSO under enhanced greenhouse conditions. Therefore, the role of global warming in altering the strength and periodicity of ENSO and the extent of ENSO's effect on global temperatures are questions of foremost importance (Angell 2000). These issues can be addressed with the help of CGCMs as they provide controlled experiments to assess separately the natural variability of the climate system and the variability caused by anthropogenic influences. The ability of these global models to simulate natural variability like ENSO is therefore of vital importance.

Tropical Pacific variability, and specifically the simulation of ENSO in CGCMs has previously been assessed in many studies, including McCreary and Anderson (1991), Neelin et al. (1992), Mechoso et al. (1995), and more recently through the El Niño Simulation Intercomparison Project (ENSIP, Latif et al. (2001)) and the Study of Tropical Oceans in Coupled models (STOIC, Davey et al. (2001)). Delecluse et al. (1998) provide a comprehensive review of the development of coupled models as they relate to ENSO behavior. The present study compares "fully global"

coupled ocean-atmosphere models that include (either prognostic or diagnostic) sea-ice. The objective in this study is not to rank each model's performance, but to describe their relative strengths and weaknesses in simulating the mean state, annual cycle and ENSO variability in order to explore possible causes for the quality of their ENSO simulations.

Individual CGCMs included in the present study have also been studied by other authors under control and enhanced CO_2 conditions and have been found to have varying capabilities for simulating ENSO. For example, Knutson et al. (1997) discuss the ENSO simulation and its sensitivity to CO_2 in the GFDL R15a model analyzed here. They find that the amplitude of the model simulated ENSO is weaker than observed but qualitatively captures the delayed oscillator mechanism of ENSO despite its coarse ocean resolution. They also found that under CO_2 doubling and quadrupling, there is a slight decrease in amplitude comparable to the magnitude of interdecadal changes. Lau et al. (1992) using a similar model that uses annually averaged insolation found that the model exhibits well-defined fluctuations in the tropical Pacific with a preferred time-scale of 3-4 years. They also found some aspects of the model behaviour during warm and cold episodes similar to observed ENSO phenomena. The ECHAM4/OPYC3 model is described by Roeckner et al. (1996) as being able to capture features of the observed interannual SST variability such as amplitude, lifetime and frequency of occurrence of El Niño events and also the phase locking of SST anomalies to the annual cycle. Bacher et al. (1998) using the same model found pronounced tropical eastern and central Pacific interannual variability. Although the model captures the essential dynamics of ENSO, the SST variability represented by a single broadband maximum of power spectral density centered at 28 months. Oberhuber et al. (1998) used the same model in predictive mode utilizing data assimilation to generate the subsurface thermal structure to successfully hindcast the 1997-98 El Niño event with slightly reduced amplitudes. Timmermann et al. (1999) and Roeckner et al. (1999) discuss the model under various forcing scenarios and the implications for future climate. The former found that year to year variability becomes more extreme under enhanced greenhouse conditions with evidence to suggest that strong cold extremes become more frequent. Yukimoto et al. (1996, 2000) found that the MRI model reveals interannual variability in the tropical Pacific which has several characteristics typical of the observed ENSO and captures the delayed oscillator mechanism of ENSO. Meehl and Arblaster (1998) found spatial patterns in the NCAR Climate System model (NCAR-CSM) similar to those

associated with the Southern Oscillation. They also found that the model produces about 60% of the observed variability in the SSTs of the NIÑO3 region. Another NCAR model (NCAR-WM) considered in this study has been examined for ENSO behavior under enhanced CO_2 conditions (Meehl and Washington (1996)). They found a reduction of east-west or zonal gradient along the equatorial Pacific similar to that seen during El Niño events. They however did not find any significant changes in El Niño frequency between control and enhanced CO_2 experiments. Tett (1995) found that the HadCM2 flux-corrected model has an oscillation that is qualitatively similar to that of the observed ENSO. Tett et al. (1997) found that the same model shows significant spectral peaks at the ENSO time-scales and shows strong regressions with central Pacific temperatures and near surface temperatures over most of the tropics and similarities to observed EOF patterns and explained variability. Collins (2000) examined its response to CO_2 increase and found that no significant changes in ENSO are seen until those levels approach four times preindustrial values. Quadrupled CO_2 levels in the model yielded ENSO events of 20% larger amplitude, doubled frequency and phase locking to annual cycle at a different time of year. The newer HadCM3 model that does not employ flux corrections has been examined by Collins et al. (2001), finding that the simulated ENSO has an amplitude within the range of uncertainty in the observations.

These previous studies of ENSO in GCMs have concentrated on SST variations in the tropical Pacific, and discussions of the atmospheric response have been limited to east- west movements of the convergence zone. In this study, we investigate the range of simulated atmospheric responses to ENSO events, and apply a uniform method of analysis to all of the models.

The model data are discussed in Section 2, and the validation data are discussed in Section 3. In Section 4.1 the equatorial Pacific climatology and variability is discussed, and in Section 4.2 ENSO indices are presented. The relationship between the pressure and temperature indices are discussed in Section 4.3, and in Section 4.4 phase locking of ENSO to the seasonal cycle, and tropical and extratropical ENSO behaviour is discussed. Conclusions are given in Section 5.

2. The Models

Control simulations from 17 global coupled ocean-atmosphere general circulation models (CGCMs) from CMIP (Meehl et al. (2000)) are studied. These models typically represent a mid-to-late 1990s vintage and may not represent the capabilities of more recent versions. Here we analyze 80 years of monthly mean surface air temperature(TAS), sea-level pressure(PSL), and precipitation(PR), the only variables in the archive for which monthly time series were supplied. Table 1 shows the coupled models and the salient features of their component ocean and atmosphere models. Ten of the models employed “flux adjustment” (Sausen et al. (1988)). Individual ocean model horizontal resolutions range from 0.67° x 0.67° to 4° x 5° and from 11 to 45 levels in the vertical. The ocean models typically use the primitive equations with a range of assumptions (of incompressibility and of hydrostatic and Boussinesq approximations, use or neglect of momentum advection, "rigid-lid" upper boundary or "free surface" condition, etc.). Atmospheric models range in resolution from R15 (4.5° x 7.5°) with 9 layers in the vertical to T42 (2.8° x 2.8°) with 19 levels. The reader is referred to the web site http://www-pcmdi.llnl.gov/cmip/ for more details. The model data (with the exception of ECHAM4/OPYC3) were gathered under CMIP-2. The ECHAM4/OPYC3 data is the first 80-year subset of the 240-year control run data available from the IPCC Data Distribution Center (http://ipcc-ddc.cru.uea.ac.uk).

A subset of the models studied here were also used in the ENSIP and STOIC intercomparisons (Latif et al. (2001) and Davey et al. (2001), respectively). These include BMRC, CCMA, ECHAM3/LSG, ECHAM4/OPYC3, GFDL, MRI, LMD/IPSL, NCAR-CSM, NCAR-WM and HadCM3. The CMIP2 runs for MRI, BMRC, CCSR and CERFACS use model versions different from the ENSIP and STOIC analyses. Here, BMRC and CCSR are flux-corrected, and CERFACS employs a global ocean model. The CMIP models, CSIRO, IAP/LASG, HadCM2, GISS and DOE-PCM, were not examined in ENSIP or STOIC. For the remaining models our results complement the ENSIP and STOIC analyses, but some differences in statistics arise since we analyzed 80 years of data, while they typically analyzed a 20-year segment from each of the coupled models.

3. Validation Data

To gain a sense of observational uncertainties, we have used several different data sources. These include the 50-year NCEP reanalysis (Kalnay et al. (1996)) and the 15-year ECMWF reanalysis (ERA15, Gibson et al. (1997)). The NCEP reanalysis covers the period 1949-1998, while ERA15 covers the shorter period from 1979-1993. A subset of the NCEP reanalysis for the same years (1979-1993) was also considered (hereafter referred to as NCEP15) to provide a direct comparison against ERA15.

The Hadley Ice and Sea Surface Temperature (HadISST) version 1.1 dataset (Rayner et al., (2000, 2001)) for the 1871-1999 period is used to enable an evaluation of the model runs in the context of interdecadal ENSO variability. We have also used the observed Darwin and Tahiti sea-level pressures covering the period 1855-2000 (available from Climatic Research Unit (CRU) of the University of East Anglia). Allan et al. (1991) and Können et al. (1998) provide details of the early pressure sources and methods used to compile this timeseries.

4. Results

Numerous authors have suggested the importance of properly simulating the mean climatology of the equatorial Pacific for achieving realistic interannual variability (Zebiak and Cane (1987), Schopf and Suarez (1988), Battisti and Hirst (1989), and Neelin (1991)). However, intercomparison studies by Neelin et al.(1992), Mechoso et al. (1995), and Latif et al.(2001) concluded that the simulation of ENSO variability in CGCMs seems to be relatively unaffected by the base state of the model or by the behavior of the simulated seasonal cycle. We will investigate this question, as well as the ability of the models to simulate phase locking of ENSO with the seasonal cycle and their ability to capture global teleconnections associated with ENSO.

4. 1 Mean climatology and variability in the equatorial Pacific

Figure 1a shows the climatological mean surface air temperature (TAS) across the equatorial Pacific (averaged between 2^{o}N-2^{o}S). The TAS is compared to the sea surface temperature (SST) from HadISST 1.1. TAS from the reanalyses serves as a good proxy for SST as the month

to month variabilities of these two timeseries are highly correlated (R~0.98). Among the observational datasets, ERA15 is consistently about 1ºC warmer than NCEP, whereas HadISST 1.1 SST is closer to NCEP SST in the east and to ERA15 SST in the west. Overall the observed uncertainty in TAS is about 1°C. Clearly the model spread is outside the observed range of TAS, but the models are capable of simulating the temperature gradient across the Pacific associated with the warm pool in the western Pacific and the cold tongue of the eastern Pacific. The spread is much larger among the models that do not employ flux correction (represented by colored dashed lines in this and all line plots in this study), while the flux-corrected models are clustered closer to the observed data. The simulated TAS gradients in the portion of the Pacific where the gradient is linear are fairly good, but near the continental edges the differences from the observations are consistent with previous studies (Mechoso et al. (1995), Davey et al. (2001), Latif et al. (2001)).

The standard deviations of the simulated and observed TAS (SST in the HadISST 1.1 data) were calculated after removing the climatological annual cycle from the 2^{o}N-2^{o}S average monthly values. The values thus obtained are plotted in Fig. 1b. The observations all show minimum variance over the western Pacific, with maximum variance in the eastern portion of the basin. In the eastern Pacific, ERA15 significantly overestimates the TAS variability relative to the NCEP reanalysis, with the NCEP reanalysis being more consistent with satellite based Microwave Sounding Unit (MSU) data, especially in the tropics (Trenberth et al. 2001). A complete analysis of the differences leading to this discrepancy and their causes is needed, but is beyond the scope of this study. While the observations show increasing variability to the east, most of the models systematically underestimate the variability in the eastern Pacific. With the exception of ECHAM4/OPYC3, the models with the most realistic variability in the eastern Pacific (HadCM3, CERFACS, and DOE- PCM) do not employ flux correction. The majority of these models have maximum standard deviation near 120^{o}W. However, their variability decreases towards the eastern edge of the Pacific Ocean unlike the observations. HadCM3 tends to be overactive across the whole basin. The models other than the ones listed above with the exception of LMD/IPSL show peak variability in the central Pacific, and in the case of NCAR- CSM in the western Pacific.

Figure 2 shows the seasonal cycle of TAS for observations (SST in the case of HadISST 1.1) and models averaged over the region 2^{o}N-2^{o}S (shown as deviations from the annual mean values in Figure 1(a)). Flux corrected models are generally able to simulate the amplitude and

phase of the seasonal cycle well except in the case of GFDL-R15a and IAP/LASG where the westward propagation is not captured. In ECHAM4/OPYC3 the strongest anomalies appear too far west, however it must be noted that flux-correction was applied annually rather than monthly. Non-flux-corrected models exhibit weaker amplitudes and have more problems achieving the correct phasing. Among the non-flux-corrected models, HadCM3 and CERFACS do a good job of capturing the timing of the annual cycle in the eastern and central Pacific. CERFACS is better at capturing the semi-annual cycle in the western Pacific. DOE-PCM and NCAR-CSM incorrectly have semi-anual cycles in the eastern Pacific, and do not properly capture the phase of the westward propagation. In the NCAR-WM model, the phasing is delayed and the westward propagation rate is too fast, with anomalies penetrating too far to the west. LMD/IPSL fails to capture the strong cooling observed in the eastern Pacific in August and September. The GISS model performs best in the eastern Pacific, though the cold anomalies do not persist late into the calendar year, and the model does not capture the semi-annual cycle in the western Pacific, instead having unrealisitc warm anomalies early in the calendar year. Mechoso et al. (1995) and Latif et al. (2001) have noted coupled models' difficulties in simulating the seasonal cycle in the eastern tropical pacific and our findings corroborate them.

4.2 ENSO Indices

Observational studies of the El Niño Southern Oscillation phenomenon over the last few decades have employed simple indices. These indices are representative of the spatially extensive dynamic features of ENSO and are particularly useful at the peak of the ENSO events when teleconnections are strongest. Table 2 shows the climatological mean temperature (TAS in all cases except HadISST, which represents SST) and the standard deviation of the TASA (monthly anomalies with the climatological annual cycle removed) for the NIÑO3 (5^{o}N-5^{o}S, 150^{o}W-90^{o}W), NIÑO3.4 (5^{o}N-5^{o}S, 170^{o}W-120^{o}W) and NIÑO4 (5^{o}N-5^{o}S, 160^{o}E-150^{o}W) regions for the simulations and the observational data. As previously seen in Fig. 1a, the model-simulated mean TAS are as much as 3^{o}C away from observations, and even the models that employed flux correction exhibit substantial biases. A few models (CCCMA, ECHAM3/LSG, and ECHAM4/OPYC3) simulate reasonable mean temperatures across the three NIÑO regions considered, while BMRC, CERFACS and NCAR-WM tend to be too warm across the Pacific. The remaining models have a cold bias.

Table 2 reveals that few models are successful in simulating the observed variability in these regions. The peak variability in the observations is in the NIÑO3 region; a feature that is simulated by only two of the flux- corrected models (ECHAM4/OPYC3 and HadCM2). Most of the non-flux-corrected models have peak variability in the NIÑO3 region with the exception of NCAR-CSM which peaks in the NIÑO4 region, while HadCM3 has high variability in the NIÑO3.4 and NIÑO3 regions. In general, the model variability seems to not depend on the mean value of TAS in the region.

Latif et al. (1997) have discussed ENSO variations on decadal and century timescales. Figure 3(a) shows interdecadal changes in the standard deviations in the NIÑO3 region for the HadISST 1.1 and NCEP data. For both datasets the anomalies relative to the climatological annual cycle for the period of common coverage (1949-1999) were computed and the standard deviation of the monthly anomalies calculated over a moving window of 15 years length. The plot shows significant temporal changes in the standard deviation with a pronounced increase in ENSO variability from the late 1960's onwards. The early part of the SST record is characterized by decreasing NIÑO3 variability with an increasing trend in the latter portion of the 20^{th} century. For the NCEP reanalysis, the quality of the first few years of data is questionable (Kistler et al. (2001)). Importantly, thereafter the NCEP Reanalysis surface air temperature variations follow closely the interdecadal SST variability and as such the NCEP reanalysis air temperature gives reasonable bounds within which to evaluate the model surface air temperature variations. Thus, there is a wide range of observed NIÑO3 variability within which a model could be considered realistic.

Figure 3(b) shows the standard deviation of model anomalies from climatology based on the full dataset with a moving 15 year window. Even relative to the period of weakest NIÑO3 variability in the observations, standard deviation σ = 0.45°C (Fig. 3(a)), only four of the flux- corrected models (BMRC, CCSR, ECHAM4/OPYC and HadCM2) have realistic variability in the NIÑO3 region, whereas most of the non-flux-corrected models (with the exception of GISS) have reasonable variability. The models that have realistic values of the NIÑO3 variability also exhibit periods of higher variability on multi-decadal time scales, whereas the models that show consistently low values of NIÑO3 variability do not adequately simulate low frequency variability in the NIÑO3 region. Here again, HadCM2 and ECHAM4/OPYC3, and to a lesser degree CCSR

and BMRC, are the only flux-corrected models that show realistic variability, whereas among non-flux- corrected models CERFACS, DOE-PCM, and HadCM3 show interdecadal variations of the magnitude observed in the HadISST 1.1 and NCEP datasets.

An important feature of ENSO is the frequency with which it occurs. The power spectra (computed using the maximum entropy method of Burg (1967) as implemented in the SSA Toolkit described in Dettinger et al. (1995)) of the observed and model simulated NIÑO3 TASA are plotted in Fig. 4. The observed NIÑO3 TASA show a broad peak near a period of 40-50 months. Of the non-flux corrected models, HadCM3 has a realistic peak at about 40 months while peak power from CERFACS, LMD/IPSL and DOE-PCM occurs at shorter time periods than observed. The spectra of GISS, NCAR-CSM and NCAR-WM are essentially red within the ENSO band, and thus they do not have a strongly preferred interannual time-scale. Among the flux-corrected models, only the HadCM2 has peak power at observed ENSO time-scales, while ECHAM4/OPYC3 and BMRC exhibit peaks close to a 2 year period.

The Southern Oscillation Index (SOI) is the large-scale atmospheric ENSO related sea-level pressure variation. This is a basic measure of ENSO variability that models should simulate with fidelity. Following the method given by Ropelewski and Jones (1987), the SOI is calculated as the difference of standardized pressure anomalies at Tahiti and Darwin. The observed SOI is calculated using station data from Darwin and Tahiti based on the data from CRU. However, for the reanalyses and models areal averages of mean sea-level pressure over 125°E-135°E, 17°S-7°S and 155°W-145°W, 22°S-12°S (10° x 10° areas centered close to the actual locations) are used. Note, for simplicity, these regional averages will be referred to as Darwin and Tahiti respectively in this paper.

The SOI standard deviation (not shown) has an interdecadal signature similar to that of the NIÑO3 TASA standard deviations. These long term variations have been addressed in numerous studies. For example, Trenberth and Hurrell (1994) and Trenberth and Hoar (1996, 1997) discuss changes in the SOI. Evidence of changing relationships between the SOI and other variables for different periods is discussed by Elliott and Angell (1988). The present study does not address the SOI and its relationships to other variables on interdecadal time scales.

4.3 SOI and NIÑO3 teleconnections

Since Bjerknes (1966, 1969) recognized that the Southern Oscillation is connected to the warming in the eastern equatorial Pacific and provided the first plausible explanation of the dynamical phenomenon, numerous studies have shown the teleconnections or effects of the tropical Pacific warming in remote areas. The relationship between the pressure variations in the Pacific region and the warming in the NIÑO3 region have been documented in Rasmusson and Carpenter (1982). The simulation of ENSO in models (for the right reasons) and its influence in regions away from the equatorial Pacific are also important features to achieve.

Figure 5 shows the lagged correlations between the SOI and NIÑO3 TAS anomalies from the models and observations. The HadISST 1.1 SST and the CRU SOI data for the period 1871-1999 (the period of common coverage with no missing data) were used to compute the observed lagged correlations. The negative correlation indicates a negative SOI corresponding to warmer NIÑO3 temperatures. The SOI from CRU and the NIÑO3 SST from HadISST 1.1 do not exhibit a systematic lag relationship, but the reanalyses show the SOI leading the peak temperatures by up to 2 months. The peak correlation varies between the observed datasets, ranging from -0.55 to -0.7. At lag times of ±20 months the correlations exhibit their peak positive values (~0.25), signifying a composite life cycle of about 40 months, consistent with the power spectrum in Fig. 4. For the models, the link between the SOI and NIÑO3 is weaker than observed, with all failing to achieve the strong negative correlation near zero lag seen in the observations. HadCM2, HadCM3, ECHAM4/OPYC3 and CERFACS are most consistent in representing the observed lead/lag relation. However, the lifetime of an ENSO event in the ECHAM4/OPYC3 and CERFACS models is shorter than observed, with the peak positive correlation occurring at approximately ±13 months. The CCCMA and CCSR models both have their most negative correlations near lag zero, but fail to capture the positive correlations, even at lags of ±24 months. All of the other models have very weak or a consistently negative correlation at all lags indicating a weaker than observed SOI/NIÑO3 relationship. This error can be due to weak coupling between the ocean and atmosphere and/or displacements in the teleconnection patterns associated with errors in the mean state.

4.4 Composites of ENSO events

a) Seasonal cycle phase locking

While the NIÑO3 standard deviations provide an indication of the amplitudes of ENSO events, and the lagged correlations presented in the previous section reveal the nature of the relationship between the SOI and the NIÑO3 index, they do not provide any information regarding the phase locking of ENSO with the seasonal cycle. This similarity in phasing of individual events, as described in Rasmusson and Carpenter (1982), shows that while the amplitudes of El Niño episodes vary, their phasing can be remarkably similar in that the peak SST anomalies occur in the boreal winter.

The phase-locking with the seasonal cycle can be seen by plotting the standard deviation of TASA for each calendar month. As seen in Fig. 6, the observed peak interannual activity occurs during the boreal winter. However, most models do not capture the proper seasonality in their ENSO cycle. Only ECHAM4/OPYC3, HadCM2, and HadCM3 capture the pronounced winter maximum, though the latter model tends to overestimate the overall level of variability. CERFACS also has strong variability in the boreal winter, but it overestimates the variability during summer and autumn. LMD/IPSL has a tendency for a winter maxima, but the variance is relatively weak. Most of the remaining models exhibit little seasonal preference, but BMRC, CCSR and DOE/PCM exhibit a summer/late summer maximum, though they have secondary winter maxima.

To clearly depict the El Niño and La Niña events we require a consistent ocean/atmosphere response. Since phase-locking with the seasonal cycle is a basic feature of observed ENSO (Fig. 6) we will composite ENSO events based on DJF seasonal anomalies of NIÑO3 TAS and SOI. To be classified as a warm (cold) event, it is required that the standardized NIÑO3 TASA be ≥ 0.6 (≤ -0.6) and the standardized SOI be ≤ -0.6 (≥ 0.6).

Following Rasmusson and Carpenter (1982), the year preceding the anomalous DJF season is denoted “year 0”. The time evolution of monthly NIÑO3 TASA composites are plotted separately for warm and cold events in Figs. 7 (a) and (b), where we have used the HadISST 1.1 data and the CRU SOI to form the observed composites. The shaded area in each figure denotes the

one standard deviation envelope of the observed NIÑO3 SSTA evolution from the HadISST 1.1 dataset. The phase locking of the warm and cold events with the seasonal cycle is readily seen in the observations. The peak of the event occurs in winter of year(+1), with the initial warming occurring in the boreal spring of year(0), and the decay of the warm event well underway by summer of year(+1).

Many of the models do not show pronounced phase locking in the temperature evolution, and they tend to lie outside the envelope of observed events in the boreal winter of year(+1). These models also do not show the transition from negative to positive anomalies seen in the observed datasets. The models that are most consistent with the observations are BMRC, CCSR, ECHAM4/OPYC3, HadCM2 (flux-corrected models) and CERFACS, DOE- PCM, HadCM3 (non-flux-corrected models). The CCSR composite event shows a realistic positive temperature anomaly for the winter months, but does not show the negative anomalies that occur during the early and late stages of the composite event. The same models that show the most realistic warm event evolutions also show cold events that compare best with observations (Fig. 7b). These are the models that showed the most realistic phase-locking with the seasonal cycle (Fig. 6). The remaining models poorly represent the growth and decay of the warm and cold events, consistent with their lack of ability to phase-lock with the seasonal cycle.

b) El Niño Response

To examine the global atmospheric response at the peak of ENSO the DJF seasonal anomalies of the TAS, PSL and PR fields for individual warm and cold events were computed over the entire globe based on the events used to generate the composites in Fig. 7a. The composite of warm events for the NCEP reanalysis is shown in Fig. 8. (Spatial composites of El Niño events and DJF season climatologies for all the reanalyses and models analyzed here can be found at http://www-pcmdi.llnl.gov/krishna/CMIP_ENSO). The three panels show the spatial fields for which warm-event composites were constructed. Hoerling et al. (1997) have discussed the nonlinear nature of the response due to El Niño and La Niña events which is not addressed here.

Figure 8 shows the salient features of the composite warm event anomalies for the DJF season, the period of maximum ENSO forcing (Fig. 6). The NCEP patterns of TAS and PSL over the

Pacific and Indian Oceans are similar to ERA15 and NCEP15, but with reduced amplitude due to the longer record employed and the associated interdecadal ENSO variations seen in Fig. 3a.

The dramatic perturbation to the Walker circulation and the warm TAS anomalies in the tropical Pacific give rise to large-scale changes in the distribution of rainfall, especially in the tropics. The positive anomaly of precipitation over the tropical Pacific extends from the dateline to the coast of South America, although the magnitude of the enhanced rainfall varies among the reanalyses. Additionally, there is evidence of an eastward displacement of the South Pacific Convergence Zone (SPCZ). Other features common to all reanalyses are the positive rainfall anomalies in the tropical Indian Ocean and in the extratropics adjacent to the west coast of North America. However, discrepancies exist in the west Pacific and elsewhere.

In the Pacific Ocean, the dateline is a key region for the anomalies of TAS, PSL and PR. Specifically, this is the location of transition for Walker circulation anomalies; to the east of the dateline the largest positive TAS and PR anomalies are found. With these robust features of ENSO in mind, we find that the simulated warm event composites can be categorized into three groups based upon common features in the composites. A representative model from each group is shown in Figs. 9-11.

Group 1: ECHAM4/OPYC3, HadCM2(shown in Fig. 9), CERFACS, DOE-PCM, and HadCM3 are most consistent with observations. Notably, they have well defined Walker circulation anomalies, with enhanced TAS anomalies extending from the tropical central Pacific to the west coast of South America. As seen in Table 2 these models also have reasonable variability of the NIÑO3, NIÑO3.4, and NIÑO4 TAS anomalies. These models also simulate well the associated El Niño rainfall in the tropical Pacific, although HadCM3 exhibits a westward extension of the rainfall and TAS to 150°E in conjunction with its westward equatorial extension of negative PSL anomalies near the equator (not shown).

Group 2: BMRC (shown in Fig. 10), CCSR, NCAR-CSM, and NCAR-WM are characterized by a westward displacement of the Walker circulation anomalies. CCSR is an exception in that although the location and magnitude of the positive PSL anomalies are more realistic, the maximim TAS anomalies are in the central/western Pacific. In the remaining models, positive PSL anomalies >0.5hPa extend to only ~150°E in the tropical Pacific. The maximum TAS warming is

located in the tropical central Pacific Ocean, while the anomalies closer to South America are decidedly weaker than observed. Consistent with enhanced surface temperatures in the central Pacific is the presence of positive rainfall anomalies. Unlike the observations, the enhanced rainfall of >0.5mm day^{-1} fails to extend to the eastern equatorial Pacific, consistent with the westward displacement of temperature and the Walker circulation anomalies.

Group 3: CCCMA (shown in Fig. 11), CSIRO, ECHAM3/LSG, GFDL, GISS, IAP/LASG, LMD/IPSL, and MRI underestimate positive PSL anomalies in the western Pacific. The positive TAS anomalies in the central/eastern tropical Pacific are severely underestimated in all of these models except MRI and LMD/IPSL. These models have their strongest positive rainfall anomalies at/or west of the dateline.

We find that models in the first group have the most realistic TASA standard deviations in the three NIÑO regions considered, that is maximum in NIÑO3 and weaker to the west (except HadCM3-same in NIÑO3 as NIÑO3.4) and overall the most realistic amplitudes. Models exhibiting the westward shift of the PSL Walker circulation anomalies (Groups 2 and 3) have the weakest TAS anomalies in NIÑO3. Only 3 models in either group has peak variability in the NIÑO3 region, but it is much weaker than observed. In examining the precipitation climatologies for the DJF season (not shown here; please refer to http://www-pcmdi.llnl.gov/krishna/CMIP_ENSO), the models with the most realistic precipitation response (models of Group 1) also have the most realistic climatology. However, other models with realistic climatological DJF precipitation do not show a realistic response to warm events. If we examine Fig. 2 in this context, it can be seen that the ability of models to simulate the annual cycle of TAS in the equatorial Pacific does not affect the models' ability to simulate a realistic ENSO response. This is consistent with the findings of Neelin et al. (1992), Mechoso et al. (1995) and Latif et al. (2001).

c) Extratropical Teleconnections

The displacement of warm surface temperature anomalies into the central Pacific, and the associated diabatic heating are known to excite the Tropical-Northern Hemisphere (TNH) teleconnection mode (Barnston and Livezey (1987), Trenberth and Caron (2000), S. Nigam (personal communication, 2000)). With respect to surface temperature, the extratropical response is characterized by warming over Canada, extending to the Great Lakes and into the northeastern United

States (Fig. 8 a). Interestingly, The models with the most realistic El Niño rainfall anomalies in the central Pacific (CERFACS, ECHAM4/OPYC3, HadCM2, DOE-PCM, and HadCM3) fail to capture the location of observed warming over North America. In CERFACS and ECHAM4/ OPYC3 the warming is displaced farther to the northeast over Hudson Bay and Greenland, whereas the other 3 models in Group 1 have cooling over much of North America. CCSR, NCAR-CSM, NCAR-WM, ECHAM3/LSG, and MRI displace the extratropical warming to the west over northwestern Canada and Alaska, consistent with their main center of diabatic heating being located to the west of dateline. The remaining models tend to simulate cooling over northern North America. Possible reasons for this dramatic shortcoming of the bulk of the models include incorrectly simulating the vertical profile of the diabatic heating in the tropics and/or systematic error of the base state climatologies of the upper-level flow which would preclude the propagation of the signal into the extratropics.

5. Conclusions

The CMIP models seem to be quite reasonable in simulating the TAS gradient across the equatorial Pacific, although problems near the continental margins noted in previous model studies persist. While the flux-corrected models are better at simulating the mean and annual cycle of temperature in the equatorial Pacific, they tend to underestimate the interannual variability in the NIÑO3 region, whereas non-flux corrected models seem to be better at simulating the variability. However, the role of flux-correction in simulating the interannual variability in the equatorial Pacific TASA is not clear, as numerous other factors including the convective and cloud parameterizations may also play important roles in determining the simulated variability.

The variability in selected index regions (NIÑO3, NIÑO3.4 and NIÑO4) also seems not to be affected by the climatological TAS values in those regions, indicating that the variability is not strongly dependent on the base state of the tropical Pacific SST in the models. Power spectra of the NIÑO3 TASA indicate that only a few models exhibit the observed peak near 40-50 months. These models also exhibit a large range of interdecadal variability. The models that do well in simulating NIÑO3 TASA variations also exhibit reasonable power spectra for the SOI, albeit weaker than observed.

The models with realistic variability in the NIÑO3 region also demonstrate phase locking with the seasonal cycle as seen in the seasonality of the peak variability of TAS anomalies. However, there are only a few models that have amplitudes for ENSO events within the observed range as shown by composite warm and cold events.

Composites of warm events also show the inadequacies of the models in simulating the observed spatial patterns of ENSO events. There are few models that generate realistic atmospheric responses of TAS, PSL and PR. Most models are unable to simulate realistic PSL anomalies, this being associated with problems in the location and magnitude of the ENSO related precipitation. The lack of an adequate PSL response is also the likely reason for the less-than-adequate simulation of the SOI. The simulation of the climatological seasonal mean precipitation was found to be a necessary but not sufficient condition for a realistic pattern of the precipitation response. Of the 5 models that had the most realistic global patterns of TAS, PSL and PR, four had oceanic horizontal resolutions of 1° or finer in the tropical Pacific. However, high oceanic resolution is not a sufficient condition for the proper simulation of the Pacific and/or global ENSO signal, since other models with fine oceanic horizontal resolution performed poorly in this respect. Furthermore, as discussed in Latif et al. (2001), even models with coarse horizontal resolution are capable of simulating delayed-oscillator physics.

Further studies with data not currently available from CMIP, such as wind speed/stress, sea surface temperature and ocean thermocline depth at monthly or shorter timescales, are necessary to diagnose the causes and relationships involved in the simulation of ENSO. Efforts are underway to collect these and other data from the CMIP runs under an augmentation of the CMIP2 database.

Acknowledgements: The authors are thankful to Kevin Trenberth and one anonymous reviewer for suggestions that helped improve this manuscript. The authors also wish to acknowledge the comments and suggestions provided by Curt Covey and the CMIP modelling group representatives. We owe thanks to Clyde Dease of the PCMDI computations staff for assistance with data processing. This work was performed under the auspices of the U.S. Department of Energy by University of California Lawrence Livermore National Laboratory under contract No. W-7405-ENG-48.

References

Allan RJ, Nicholls N Jones PD and Butterworth IJ (1991) A further extension of the Tahiti-Darwin SOI, early SOI results and Darwin pressure. J Clim 4: 743-749

Angell JK (1990) Variation in global tropospheric temperature after adjustment for the El Niño influence, 1958-89. Geophys Res Lett 17: 1093-1096

Angell, JK (2000) Tropospheric temperature variations adjusted for El Niño, 1958-1998. JGR 105: 11,841-11,849

Bacher A, Oberhuber JM, Roeckner E (1998) ENSO dynamics and seasonal cycle in the Tropical Pacific as simulated by the ECHAM4/OPYC3 coupled general circulation model. Clim Dyn 14: 431-450

Barnston A, and Livezey RE (1987) Classification, seasonality, and persistence of low-frequency circulation patterns. Mon Wea Rev 115: 1083-1126

Battisti DS, and Hirst AC (1989) Interannual variability in the tropical atmosphere- ocean system: Influence of the basic state, ocean geometry, and non-linearity. J Atmos Sci 46: 1687-1712

Bjerknes J (1966) A possible response of the atmospheric Hadley circulation to equatorial anomalies of ocean temperature. Tellus 18: 820-829

Bjerknes J (1969) Atmospheric teleconnections from the equatorial Pacific. Mon Wea Rev 97: 163-172

Boden TA, Kanciruk P and Stoss FW (1990) Trends ‘91. A Compendium of Data on Global Change. Carbon Dioxide Information Analysis Center. Publ. ORNL/CDIA-36. ORNL, Oak Ridge, TN 257

Boden TA, Sepanski RJ, and Stoss FW (1992) Trends ‘91. A Compendium of Data on Global Change. Carbon Dioxide Information Analysis Center. Publ. ORNL/CDIA-49. ORNL, Oak Ridge, TN 60

Bradley RS, Diaz HF, Kiladis GN and Eishcheid JK (1987) ENSO signal in continental temperature and precipitation records. Nature 327: 497-501

Burg JP (1967) Maximum entropy spectral analysis. 37th Ann. Intern. Meeting. Soc. Explor. Geophys., Oklahoma City, Oklahoma

Collins M (2000) The El-Niño Southern Oscillation in the second Hadley Centre coupled model and its response to greenhouse warming. J Clim 13: 1299-1312

Collins M, Tett SFB and Cooper C, (2001) The internal climate variability of a version of the Hadley Centre coupled model without flux adjustments. Clim Dyn 17: 61-81

Davey M et al. (2001) STOIC: A study of coupled GCM climatology and variability in tropical ocean regions. Clim Dyn (submitted)

Delecluse P, Davey MK, Kitamura Y, Philander SGH, Suarez M and Bengtsson L (1998) Coupled general circulation modeling of the Tropical Pacific. J Geophys Res 103: 14357-14373

Dettinger MD, Ghil M, Strong CM, Weibel W and Yiou P (1995) Software expedites singular-spectrum analysis of noisy time series. Eos 76: 12

Elliott WP and Angell JK (1988) Evidence for Changes in Southern Oscillation relationships during the last 100 years. J Clim 1: 729-737

Gibson JK, Kallberg P, Uppala S, Hernandez A, Nomura A and Serrano E (1997) ERA description, ECMWF Reanalysis Project Report Series 1, European Centre for Medium Range Weather Forecasts, Reading, UK, 66

Hoerling MP, Kumar A and Zhong M (1997) El Niño, La Niña, and the nonlinearity of their teleconnections. J Clim 10: 1769-1786

Jones PD (1988) The influence of ENSO on global temperatures. Climate Monitor 17: 81-89

Kalnay E, Kanamitsu M, Kistler R, Collins W, Deavan D, Iredell M, Saha S, White G, Woolen J, Zhu Y, Leetma A, Reynolds R, Chelliah M, Ebisuzaki W, Higgins W, Janowiak J, Mo KC,

Ropelewski C, Wang J, Jenne R and Joseph D (1996) The NCEP/NCAR 40-year reanalysis project. Bull Amer Meteor Soc 77: 437-471

Kistler R, Collins W, Saha S, White G, Woollen J, Kalnay E, Chelliah M, Ebisuzaki W, Kanamitsu M, Kousky V, Dool H-V-D, Jenne R, and Fiorino M (2001) The NCEP-NCAR 50-Year Reanalysis: Monthly Means CD-ROM and Documentation. Bull Amer Meteor Soc 82: 247-268

Knutson TR and Manabe S (1994) Impact of increasing CO_2 on simulated ENSO-like phenomena. Geophys Res Lett 21: 2295-2298

Knutson TR and Manabe S (1995) Time-mean response over the tropical Pacific to increased CO_2 in a coupled ocean-atmosphere model. J Clim 8: 2181-2199

Knutson TR, Manabe S and Gu D (1997) Simulated ENSO in a global coupled ocean- atmosphere model: Multidecadal amplitude modulation and CO_2 sensitivity. J Clim 10: 138-161

Können GP, Jones PD, Kaltofen MH and Allan RJ (1998) Pre-1866 extensions of the Southern Oscillation Index using early Indonesian and Tahitian meteorological readings. J Clim 11: 2325-2339

Latif M, Kleeman R and Eckert C (1997) Greenhouse warming, decadal variability, or El Niño?. An attempt to understand the anomalous 1990s. J Clim 10: 2221- 2239

Latif M et al. (2001) ENSIP: The El Niño Simulation Intercomparison Project. Clim Dyn (in press)

Lau NC, Philander SGH and Nath MJ (1992) Simulation of ENSO-like phenomena with a low-resolution coupled GCM of the global ocean and atmosphere. J Clim 5: 284-307

McCreary JP and Anderson DLT (1991) An overview of coupled ocean-atmosphere models of El Niño and the Southern Oscillation. J Geophys Res 96:, 3125-3150

McPhaden MJ (1999) The child prodigy of 1997-1998. Nature 398: 559-562

Mechoso CR et al. (1995) The seasonal cycle over the tropical Pacific in general circulation models. Mon Wea Rev 123: 2825-2838

Meehl GA, Branstator GW and Washington WM (1993) Tropical Pacific interannual variability and CO_2 climate change. J Clim 6: 42-63

Meehl GA and Washington WM (1996) El Niño-like climate change in a model with increased atmospheric CO_2 concentrations. Nature 382: 56-60

Meehl GA and Arblaster JM (1998) The Asian-Australian monsoon and El Niño- Southern Oscillation in the NCAR climate system model. J Clim 11: 1356- 1385

Meehl GA, Boer GJ, Covey C, Latif M and Stouffer RJ (2000) The Coupled Model Intercomparison Project (CMIP). Bull Amer Met Soc 81: 313-318

Neelin JD (1991) The slow sea surface temperature mode and the fast-wave limit: Analytic theory for tropical interannual oscillations and experiments in a hybrid coupled model. J Atmos Sci 48: 584-606

Neelin JD, Latif M, Allaart MAF, Cane MA, Cubasch U, Gates WL, Gent PR, Ghil M, Gordon C, Lau NC, Mechoso CR, Meehl GA, Oberhuber JM, Philander SGH, Schopf PS, Sperber KR, Sterl A, Tokioka T, Tribbia J and Zebiak SE (1992) Tropical air-sea interaction in general circulation models. Clim Dyn 7: 73-104

Nicholls N, Gruza GV, Jouzel J, Karl TR, Ogallo LA and Parker DE (1996) Observed climate variability and change. In (Houghton JT, Meira Filho LG, Callander BA, Harris N, Kattenberg A and Maskell K, Eds.) Climate Change 1995: The IPCC Second Assessment, Cambridge University Press, Cambridge: 133-192

Oberhuber JM, Roeckner E, Christoph M, Esch M and Latif M (1998) Predicting the ‘97 El Niño event with a global climate model. Geophys Res Lett 25: 2273-2276

Philander SG (1990) El Niño, La Niña, and the Southern Oscillation.Academic Press 269 pp

Privalsky VE and Jensen DT (1995) Assessment of the influence of ENSO on annual global air temperatures. Dyn Atmos and Oceans 22: 161-178

Rasmusson EM and Carpenter TH (1982) Variations in tropical sea surface temperature and surface wind fields associated with Southern Oscillation/El Niño. Mon Wea Rev 110: 354-384

Rayner NA, Parker DE, Frich P, Horton EB, Folland CK, and Alexander LV, (2000) SST and sea-ice fields for ERA40. In Proceedings of the Second WCRP International Conference on Reanalyses (Wokefield Park, nr. Readingm UK,23-27 August 1999). WCRP-109, WMO/TD-No. 985.

Rayner NA, Parker DE, Folland CK, Horton EB, Alexander LV, and Rowell DP (2001) The global sea-ice and seasurface temperature (HadISST) and night marine air temperature (HadMAT) data sets. Manuscript in preparation.

Roeckner E, Oberhuber JM, Bacher A, Christoph M and Kirchner I (1996) ENSO variability and atmospheric response in a global coupled atmosphere-ocean GCM. Clim Dyn 12: 737-754

Roeckner E, Bengtsson L, Feichter J, Lelieveld J and Rodhe H (1999) Transient climate change simulations with a coupled atmosphere-ocean GCM including the tropospheric sulfur cycle. J Clim 12: 3004-3032

Ropelewski CF and Halpert MS (1987) Global and regional scale precipitation patterns associated with the El Niño/Southern Oscillation. Mon Wea Rev 115: 1606-1626

Ropelewski CF and Halpert MS (1989) Precipitation patterns associated with the high index phase of the Southern Oscillation. J Clim 2: 268-284

Ropelewski CF and Jones PD (1987) An extension of the Tahiti-Darwin Southern Oscillation Index. Mon Wea Rev 115: 2161-2165.

Schopf PS and Suarez MJ (1988) Vacillations in a coupled ocean-atmosphere model, J Atmos Sci 45: 549-566

Sausen R, Barthel K and Hasselmann K (1988) Coupled ocean-atmosphere models with flux correction. Clim Dyn 2: 145-163

Tett S (1995) Simulation of El Niño-Southern Oscillation-like variability in a global AOGCM and its response to CO_2 increase. J Clim 8: 1473-1502

Tett SFB, Johns TC and Mitchell JFB (1997) Global and regional variability in a coupled AOGCM. Clim Dyn 13 303-323

Timmermann A, Oberhuber J, Bacher A, Esch M, Latif M and Roeckner E (1999) Increased El Niño frequency in a climate model forced by future greenhouse warming. Nature 398: 694-696

Trenberth KE, Stepaniak DP, Hurrell J and Fiorino M (2001) Quality of the reanalyses in the tropics. J Clim 14: 1499-1510.

Trenberth KE, Branstator GW, Karoly D, Kumar A, Lau NC and Ropelewski C (1998) Progress during TOGA in understanding and modeling global teleconnections associated with tropical sea surface temperatures. J Geophys Res 103: 14291- 14324

Trenberth KE, and Caron, JM (2000) The Southern Oscillation revisited: Sea level pressures, surface temperatures and precipitation. J Clim 13: 4358-4365

Trenberth KE and Hoar TJ (1996) The 1990-1995 El Niño-Southern Oscillation event: Longest on record. Geophys Res Lett 23: 57-60

Trenberth KE, and Hoar TJ (1997) El Niño and climate change. Geophys Res Lett 24: 3057-3060

Trenberth KE and Hurrell JW (1994) Decadal atmosphere-ocean variations in the Pacific. Clim Dyn 9: 303-319

Trenberth KE (1990) Recent observed interdecadal climate changes in the Northern Hemisphere. Bull Amer Meteor Soc 71: 988-993

Trenberth KE and Shea D (1987) On the evolution of the Southern Oscillation, Mon Wea Rev 115: 3078-3096

Wigley, TML (2000) ENSO, volcanoes and record-breaking temperatures.Geophys Res Lett 27: 4101-4104

Yukimoto S, Endoh M, Kitamura Y, Kitoh A, Noda A and Tokioka T (1996) Interannual and interdecadal variabilities in the Pacific in a MRI coupled GCM. Clim Dyn 12: 667-683

Yukimoto S, Endoh M, Kitamura Y, Kitoh A, Motoi T and Noda A (2000) ENSO-like interdecadal variability in the Pacific Ocean as simulated in a coupled general circulation model. J Geophys Res 105: 13945-13963

Zebiak SE and Cane MA (1987) A model El Niño Southern Oscillation. Mon Wea Rev 115: 2262-2278

List of Tables

Table 1.

Model Name	Atmosphere Resolution	Ocean Resolution	Flux Adjustment
BMRC	R21 (3.2 x 5.6) L19	(5.85 x 2.0) L25*	Salt, Heat (Surface Shortwave)
CCCMA	T32 (3.8 x 3.8 L10	(1.8 x 1.8) L29	Heat, Water [1]
CCSR	T21 (5.6 x 5.6) L20	(2.8 x 2.8) L17	Heat, Water
CSIRO	R21 (3.2 x 5.6) L9	(3.2 x 5.6) L21	Heat, Water, Momentum
ECHAM3+LSG	T21 (5.6 x 5.6) L19	(2.8 x 2.8) L11	Heat, Water, Momentum
ECHAM4+OPYC3	T42 (2.8 x 2.8) L19	(2.8 x 2.8) L11 *	Heat, Water [2]
GFDL R15a	R15 (4.5 x 7.5) L9	(4.5 x 3.7) L12	Heat, Water
IAP/LASG	R15 (4.5 x 7.5) L9	(4.0 x 5.0) L20	Heat, Water, Momentum
MRI	(4.0 x 5.0) L15	(2.0 x 2.5) L21*	Heat, Water
HadCM2	(2.5 x 3.75) L19	(2.5 x 3.75) L24	Heat, Water
CERFACS	T31 (3.9x 3.9) L19	(2.0 x 2.0) L31**	None
GISS	(4.0 x 5.0) L9	(4.0 x 5.0) L13	None
LMD/IPSL	(1.6 x 3.8) L15	(1.0 x 2.0) L31**	None
NCAR (CSM)	T42 (2.8 x 2.8) L18	(1.2 x 2.4) L45	None
NCAR (WM)	R15 (4.5 x 7.5) L9	(1.0 x 1.0) L20	None
DOE (PCM)	T42 (2.8 x 2.8) L18	(0.67 x 0.67) L32	None
HadCM3	(2.5 x 3.75) L19	(1.25 x 1.25) L20	None

* indicates enhanced horizontal resolution near the equator.

** indicates data has been regridded to coarser than original grid.

[1] Correction varies by calendar month.

[2] Correction applied annually. (In all other cases, fixed monthly corrections are applied.)

Table 2.

Model/Obs	Mean Temperature (°C)			Standard Deviation of monthly Temperature Anomaly (°C)		
	NIÑO4	**NIÑO3.4**	**NIÑO3**	**NIÑO4**	**NIÑO3.4**	**NIÑO3**
BMRC	28.8	27.4	26.2	0.53	**0.57**	0.49
CCCMA	28.2	26.8	25.8	**0.28**	0.25	0.19
CCSR	27.1	25.7	24.5	**0.75**	0.72	0.57
CSIRO	26.8	26.0	25.0	0.22	**0.26**	0.24
ECHAM3+LSG	27.9	26.7	25.6	0.27	**0.30**	0.26
ECHAM4+OPYC3	28.3	26.8	25.4	0.45	0.79	**0.84**
GFDL R15a	24.7	23.7	22.7	0.31	**0.37**	0.34
IAP/LASG	24.8	23.6	23.1	**0.31**	0.28	0.27
MRI	27.3	25.9	25.1	**0.39**	0.33	0.34
HadCM2	26.4	25.4	24.5	0.59	0.71	**0.72**
CERFACS	29.1	28.8	28.1	0.32	0.56	**0.74**
GISS	26.5	26.2	26.0	0.19	0.24	**0.27**
LMD/IPSL	26.0	25.2	24.8	0.41	0.47	**0.52**
NCAR (CSM)	25.1	24.3	23.7	**0.47**	0.44	0.40
NCAR (WM)	30.3	29.4	28.2	0.47	0.48	**0.52**
DOE-PCM	24.5	23.2	22.5	0.62	0.82	**0.85**
HadCM3	26.7	25.6	25.4	0.80	**1.07**	1.06
HadISST version 1.1	28.3	26.9	25.7	0.55	0.76	**0.80**
ECMWF Reanalysis	28.4	27.3	26.1	0.51	0.87	**0.95**
NCEP (15 years)	27.6	26.4	25.5	0.45	0.68	**0.73**
NCEP Reanalysis	27.4	26.2	25.2	0.48	0.66	**0.74**

List of Figures

one standard deviation envelope of the observed NIÑO3 sea surface temperature anomaly for "cold" events in the HadISST 1.1 dataset.

8. December-February warm event composites of (a) Surface air temperature, (b) Sea-level pressure, (c) Precipitation from NCEP Reanalysis.

9. As Fig. 8 but for HadCM2.

10. As Fig. 8 but for BMRC.

11. As Fig. 8 but for CCCMA.

Figure 1 (a)

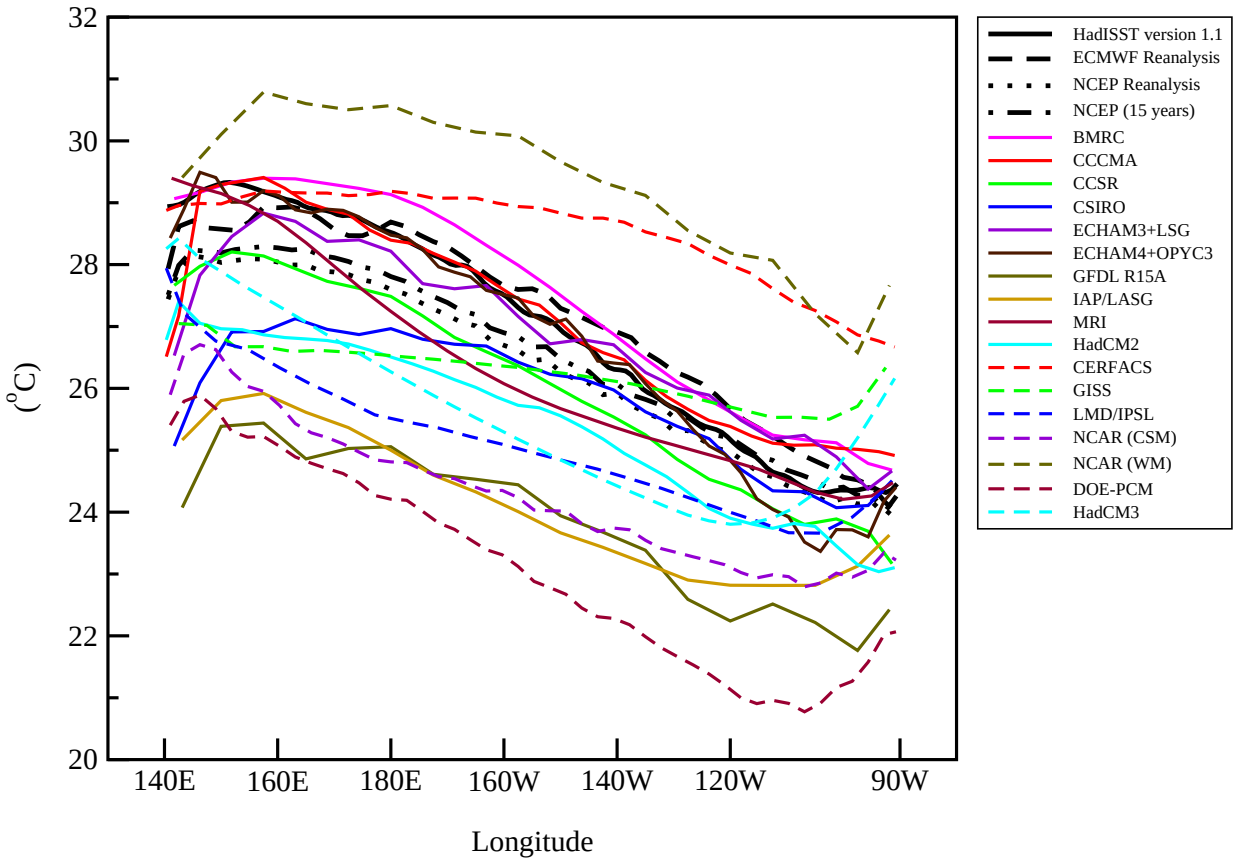
32
30
28
26
24
22
20
(°C)
140E
160E
180E
160W
140W
120W
90W
Longitude
HadISST version 1.1
ECMWF Reanalysis
NCEP Reanalysis
NCEP (15 years)
BMRC
CCCMA
CCSR
CSIRO
ECHAM3+LSG
ECHAM4+OPYC3
GFDL R15A
IAP/LASG
MRI
HadCM2
CERFACS
GISS
LMD/IPSL
NCAR (CSM)
NCAR (WM)
DOE-PCM
HadCM3

Figure 1 (b)

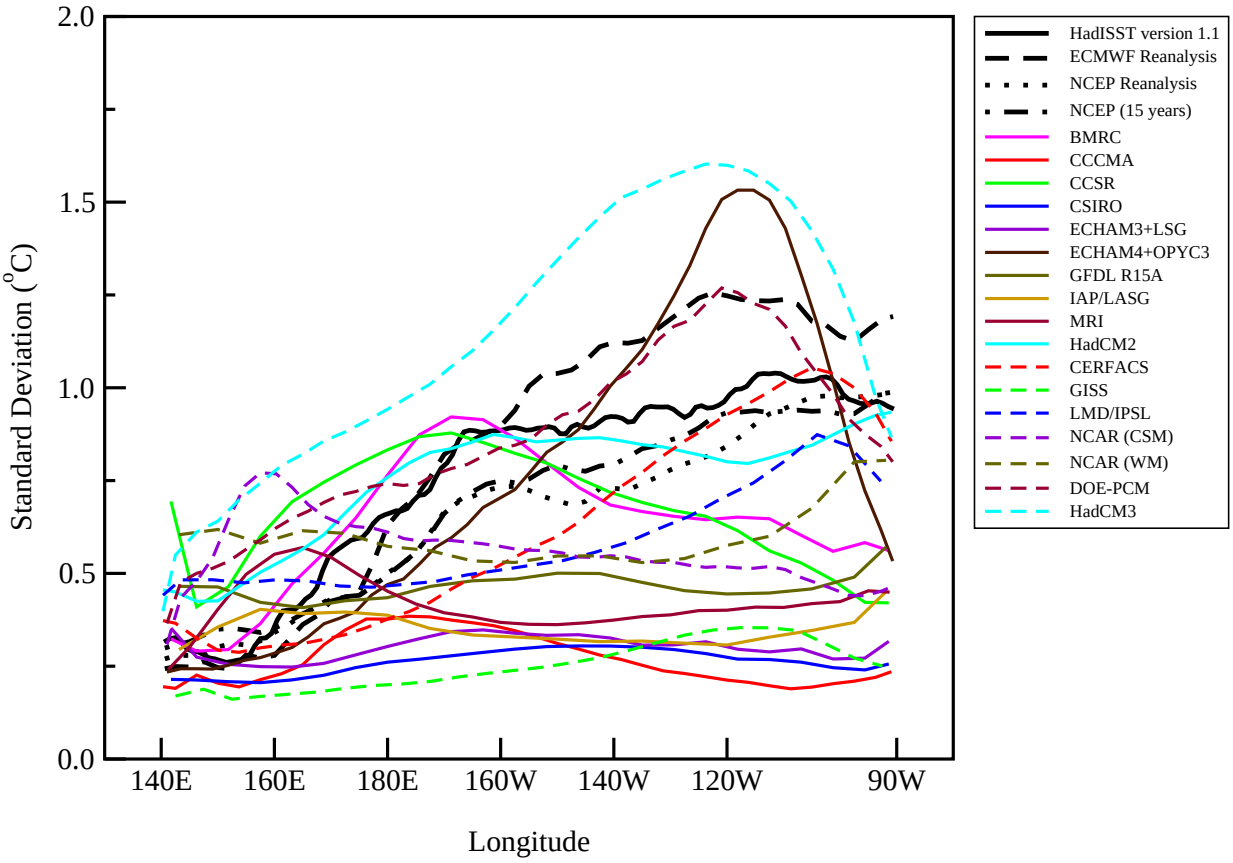
2.0
1.5
1.0
0.5
0.0
Standard Deviation (°C)
140E
160E
180E
160W
140W
120W
90W
Longitude
HadISST version 1.1
ECMWF Reanalysis
NCEP Reanalysis
NCEP (15 years)
BMRC
CCCMA
CCSR
CSIRO
ECHAM3+LSG
ECHAM4+OPYC3
GFDL R15A
IAP/LASG
MRI
HadCM2
CERFACS
GISS
LMD/IPSL
NCAR (CSM)
NCAR (WM)
DOE-PCM
HadCM3

Figure 2

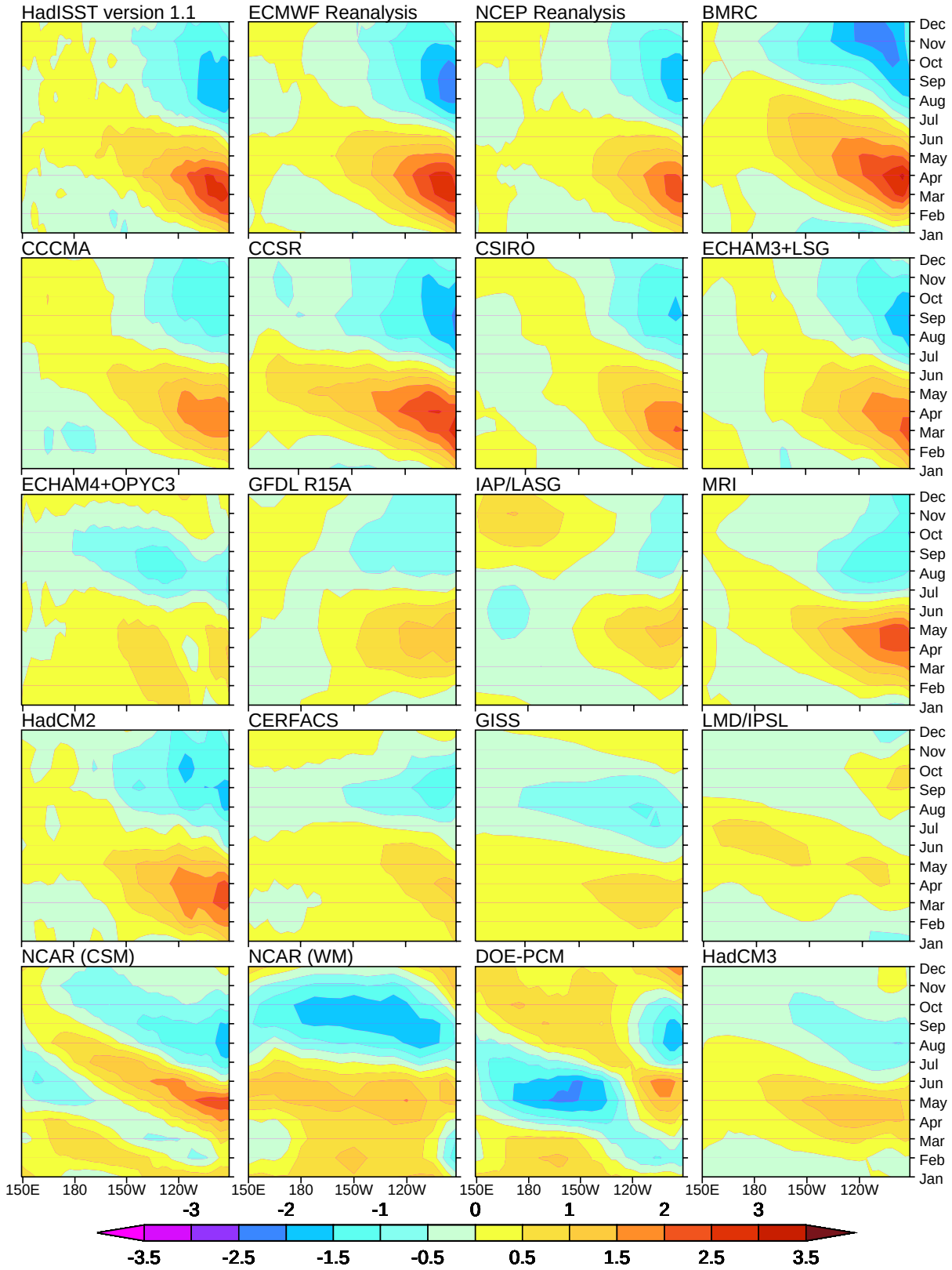
HadISST version 1.1
ECMWF Reanalysis
NCEP Reanalysis
BMRC
CCCMA
CCSR
CSIRO
ECHAM3+LSG
ECHAM4+OPYC3
GFDL R15A
IAP/LASG
MRI
HadCM2
CERFACS
GISS
LMD/IPSL
NCAR (CSM)
NCAR (WM)
DOE-PCM
HadCM3
Dec
Nov
Oct
Sep
Aug
Jul
Jun
May
Apr
Mar
Feb
Jan
150E
180
150W
120W
-3
-2
-1
0
1
2
3
-3.5
-2.5
-1.5
-0.5
0.5
1.5
2.5
3.5

Figure 3 (a)

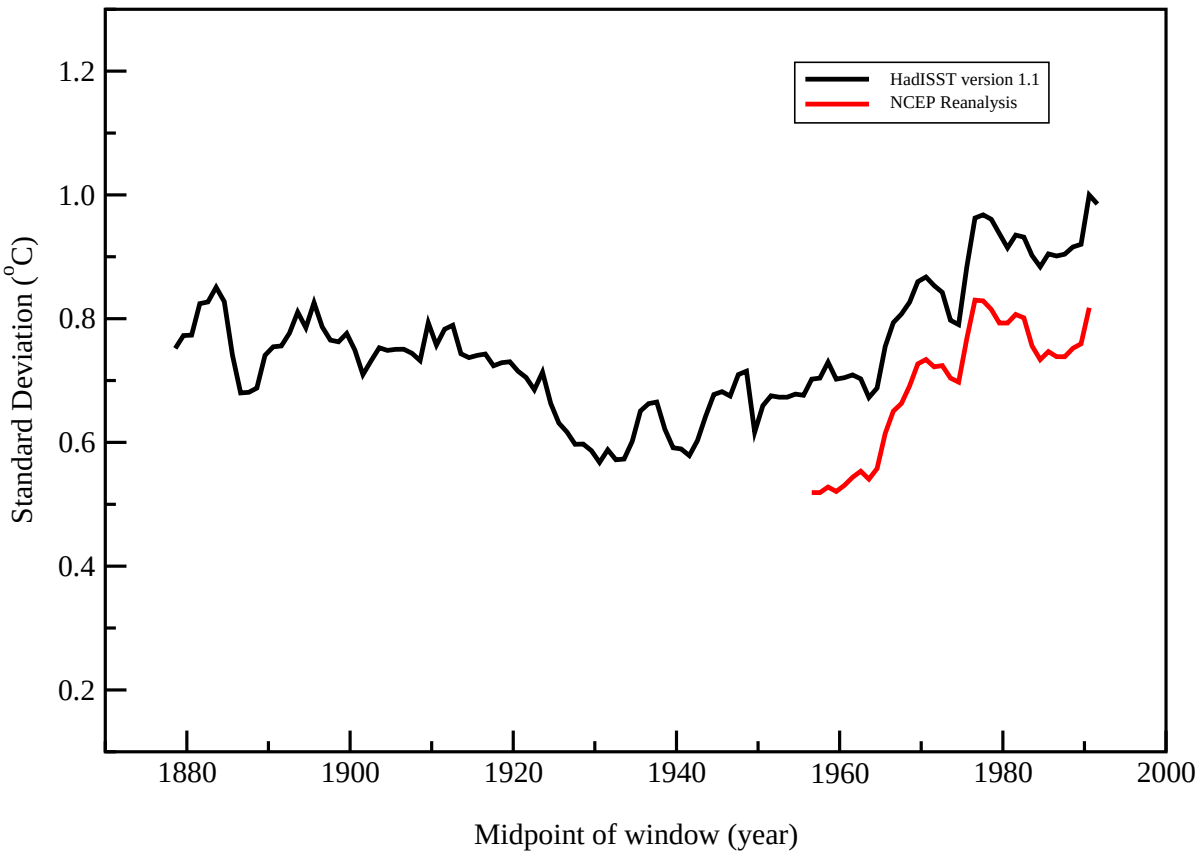
HadISST version 1.1
NCEP Reanalysis
Standard Deviation (°C)
1.2
1.0
0.8
0.6
0.4
0.2
1880
1900
1920
1940
1960
1980
2000
Midpoint of window (year)

Figure 3(b)

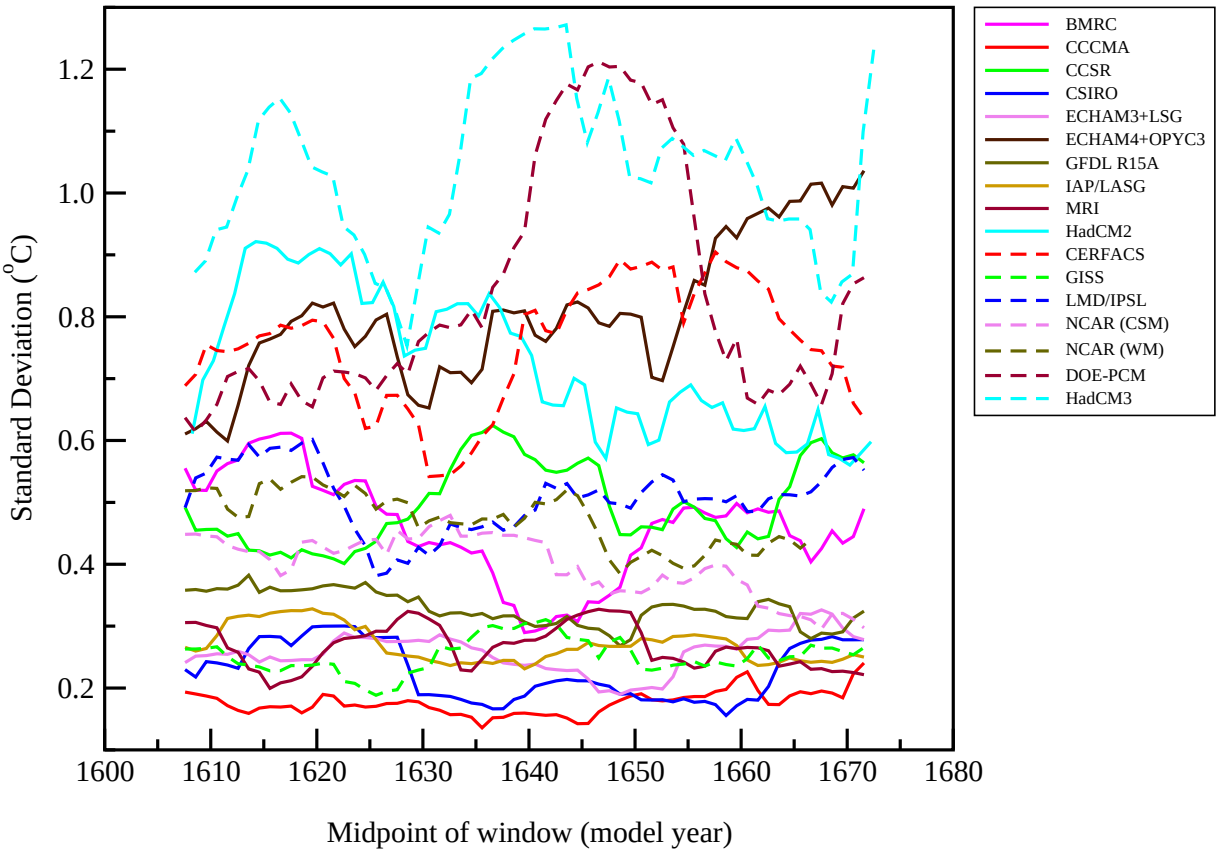
Standard Deviation (°C)
1.2
1.0
0.8
0.6
0.4
0.2
1600
1610
1620
1630
1640
1650
1660
1670
1680
Midpoint of window (model year)
BMRC
CCCMA
CCSR
CSIRO
ECHAM3+LSG
ECHAM4+OPYC3
GFDL R15A
IAP/LASG
MRI
HadCM2
CERFACS
GISS
LMD/IPSL
NCAR (CSM)
NCAR (WM)
DOE-PCM
HadCM3

Figure 4

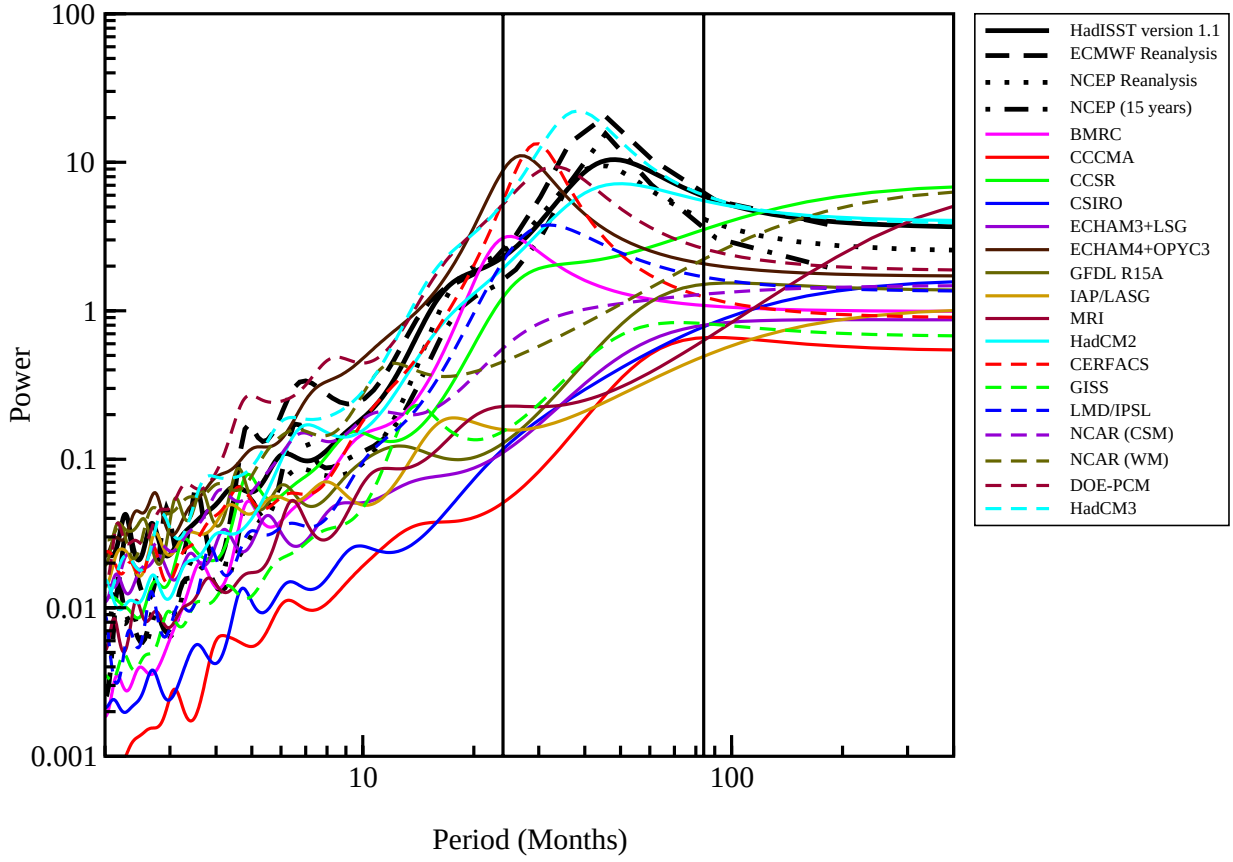
100
10
1
0.1
0.01
0.001
Power
10
100
Period (Months)
HadISST version 1.1
ECMWF Reanalysis
NCEP Reanalysis
NCEP (15 years)
BMRC
CCCMA
CCSR
CSIRO
ECHAM3+LSG
ECHAM4+OPYC3
GFDL R15A
IAP/LASG
MRI
HadCM2
CERFACS
GISS
LMD/IPSL
NCAR (CSM)
NCAR (WM)
DOE-PCM
HadCM3

Figure 5

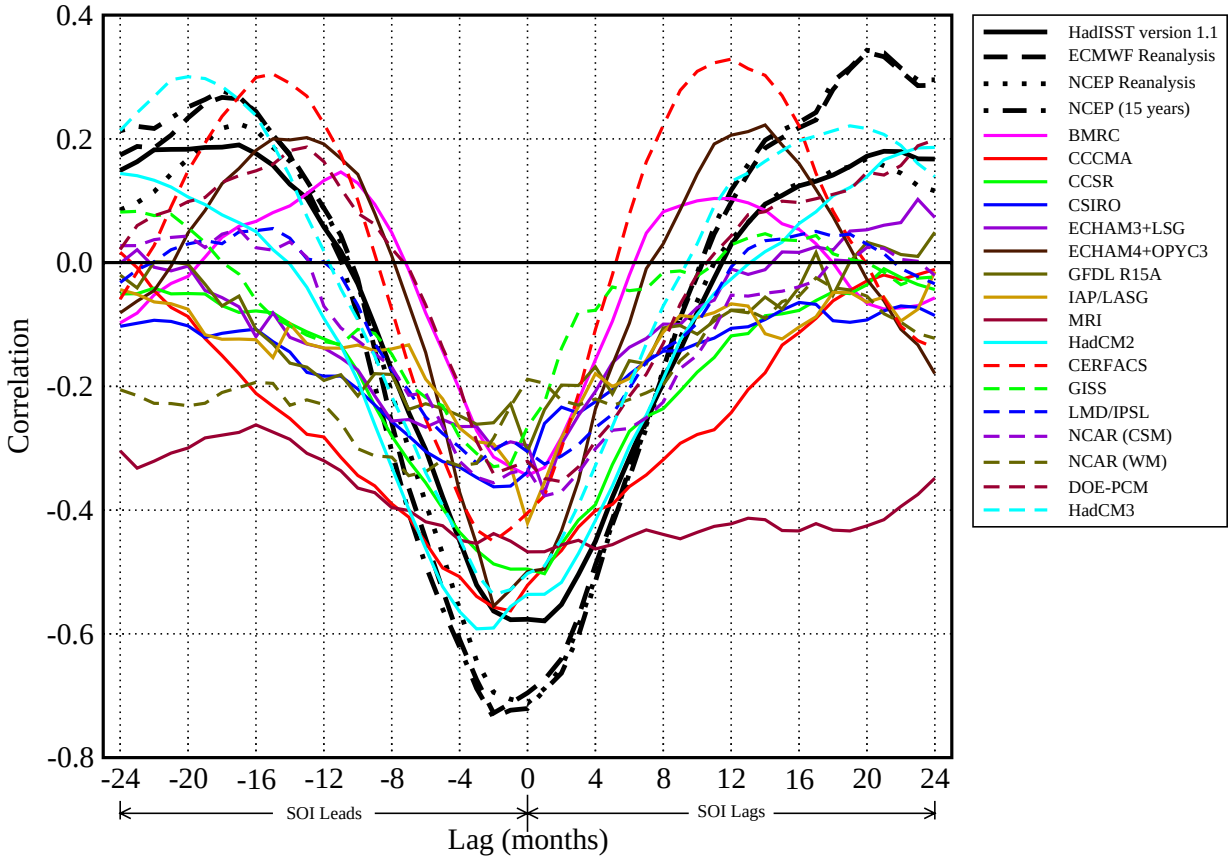
0.4
0.2
0.0
-0.2
-0.4
-0.6
-0.8
Correlation
-24
-20
-16
-12
-8
-4
0
4
8
12
16
20
24
SOI Leads
SOI Lags
Lag (months)
HadISST version 1.1
ECMWF Reanalysis
NCEP Reanalysis
NCEP (15 years)
BMRC
CCCMA
CCSR
CSIRO
ECHAM3+LSG
ECHAM4+OPYC3
GFDL R15A
IAP/LASG
MRI
HadCM2
CERFACS
GISS
LMD/IPSL
NCAR (CSM)
NCAR (WM)
DOE-PCM
HadCM3

Figure 6

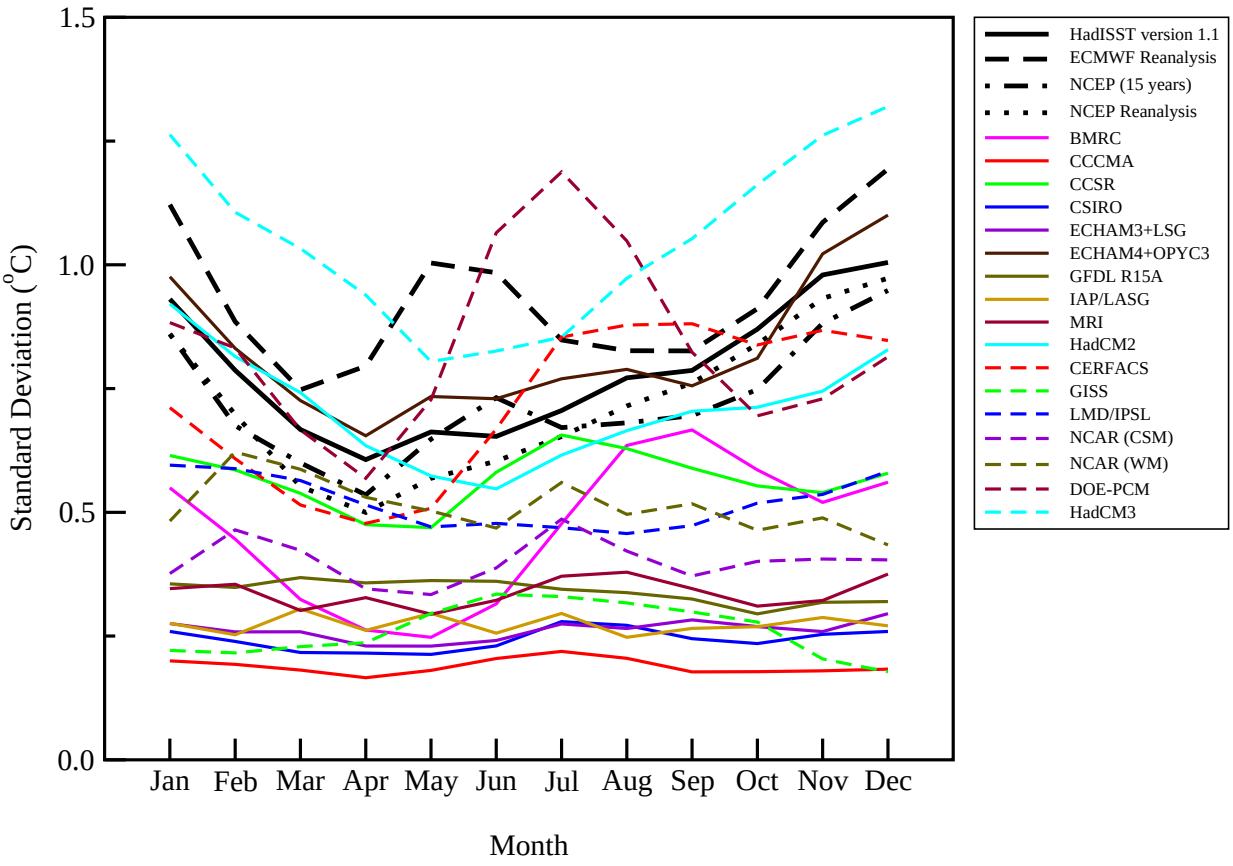
1.5
1.0
0.5
0.0
Standard Deviation (°C)
Jan
Feb
Mar
Apr
May
Jun
Jul
Aug
Sep
Oct
Nov
Dec
Month
HadISST version 1.1
ECMWF Reanalysis
NCEP (15 years)
NCEP Reanalysis
BMRC
CCCMA
CCSR
CSIRO
ECHAM3+LSG
ECHAM4+OPYC3
GFDL R15A
IAP/LASG
MRI
HadCM2
CERFACS
GISS
LMD/IPSL
NCAR (CSM)
NCAR (WM)
DOE-PCM
HadCM3

Figure 7(a)

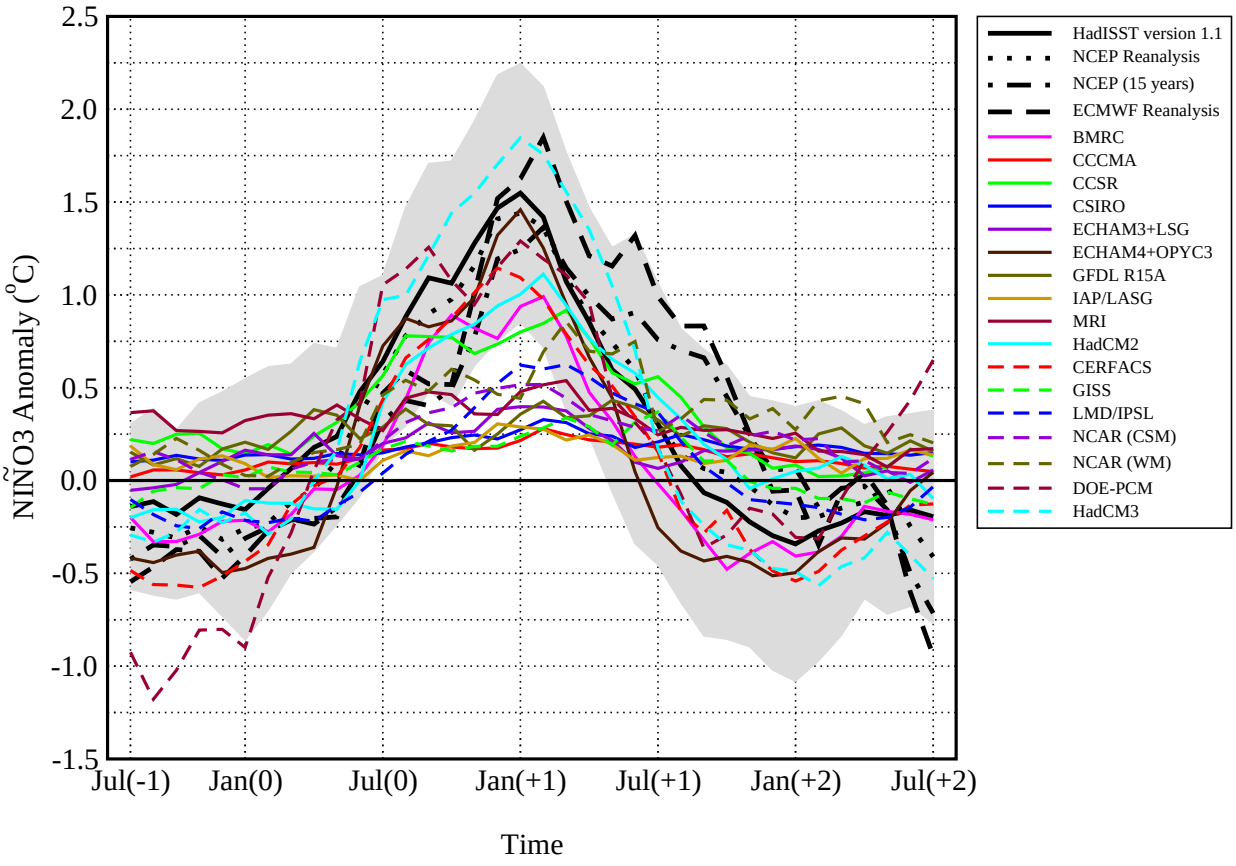
2.5
2.0
1.5
1.0
0.5
0.0
-0.5
-1.0
-1.5
NIÑO3 Anomaly (°C)
Jul(-1)
Jan(0)
Jul(0)
Jan(+1)
Jul(+1)
Jan(+2)
Jul(+2)
Time
HadISST version 1.1
NCEP Reanalysis
NCEP (15 years)
ECMWF Reanalysis
BMRC
CCCMA
CCSR
CSIRO
ECHAM3+LSG
ECHAM4+OPYC3
GFDL R15A
IAP/LASG
MRI
HadCM2
CERFACS
GISS
LMD/IPSL
NCAR (CSM)
NCAR (WM)
DOE-PCM
HadCM3

Figure 7(b)

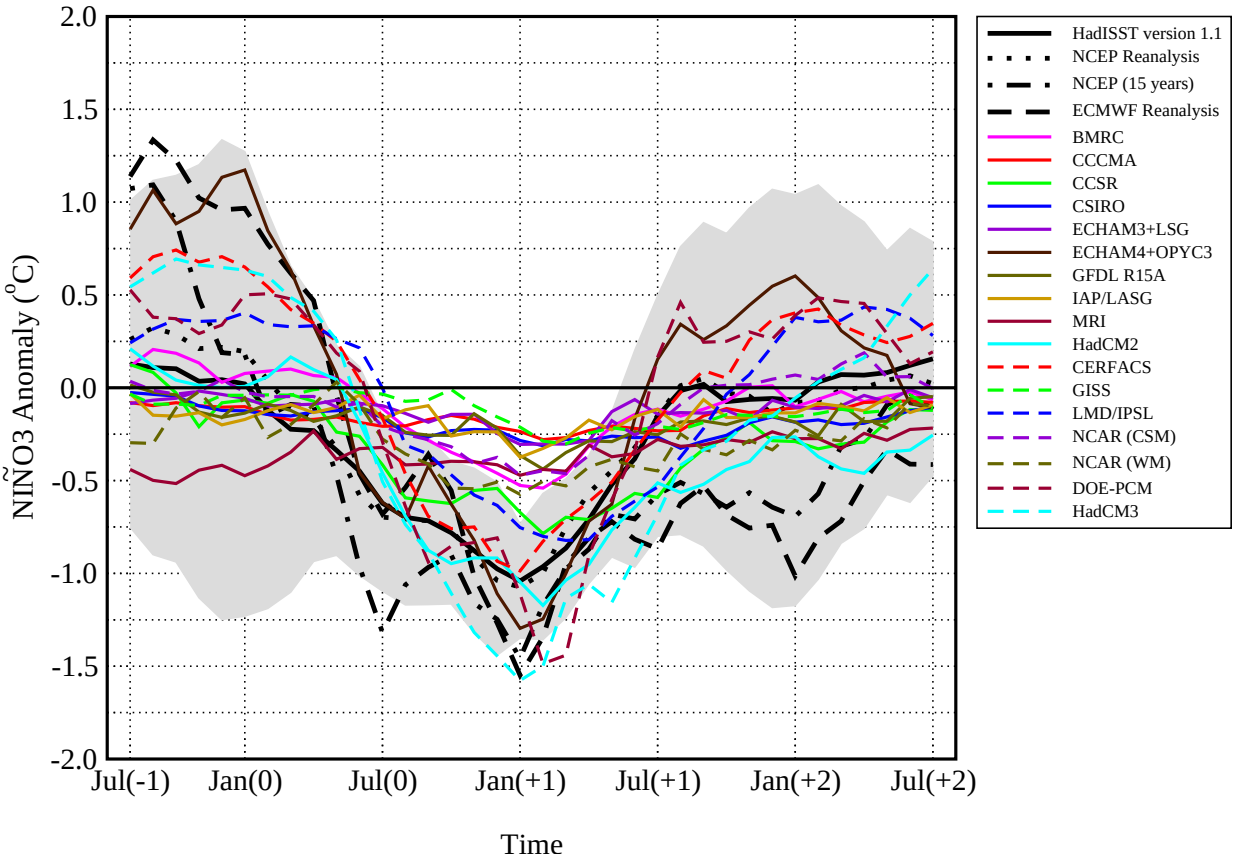
2.0
1.5
1.0
0.5
0.0
-0.5
-1.0
-1.5
-2.0
NIÑO3 Anomaly (°C)
Jul(-1)
Jan(0)
Jul(0)
Jan(+1)
Jul(+1)
Jan(+2)
Jul(+2)
Time
HadISST version 1.1
NCEP Reanalysis
NCEP (15 years)
ECMWF Reanalysis
BMRC
CCCMA
CCSR
CSIRO
ECHAM3+LSG
ECHAM4+OPYC3
GFDL R15A
IAP/LASG
MRI
HadCM2
CERFACS
GISS
LMD/IPSL
NCAR (CSM)
NCAR (WM)
DOE-PCM
HadCM3

Figure 8

NCEP Reanalysis. Warm event anomalies for DJF

(a) TAS

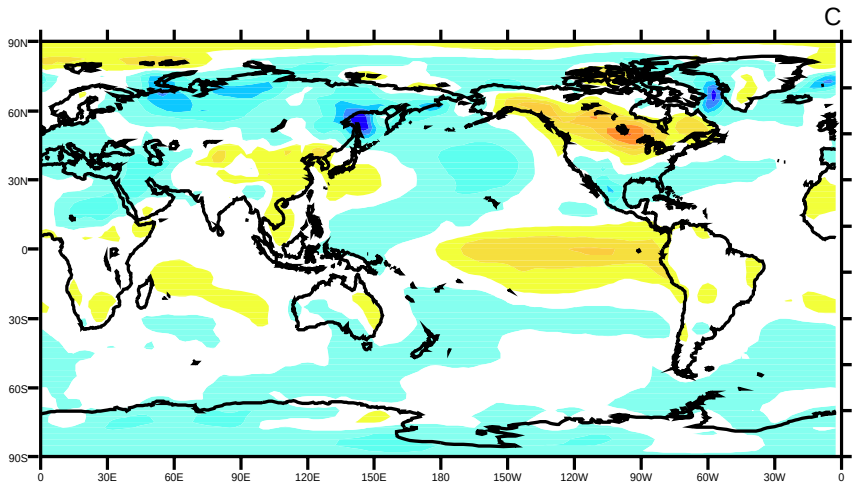

(b) PSL

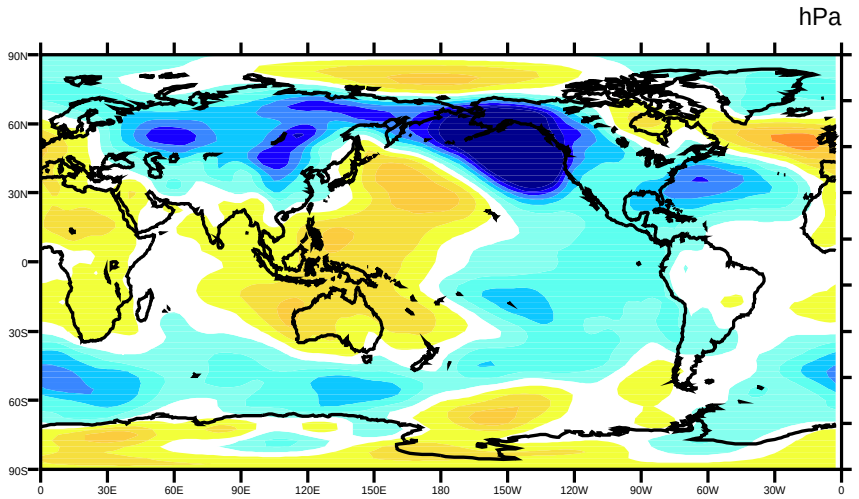

(c) PR

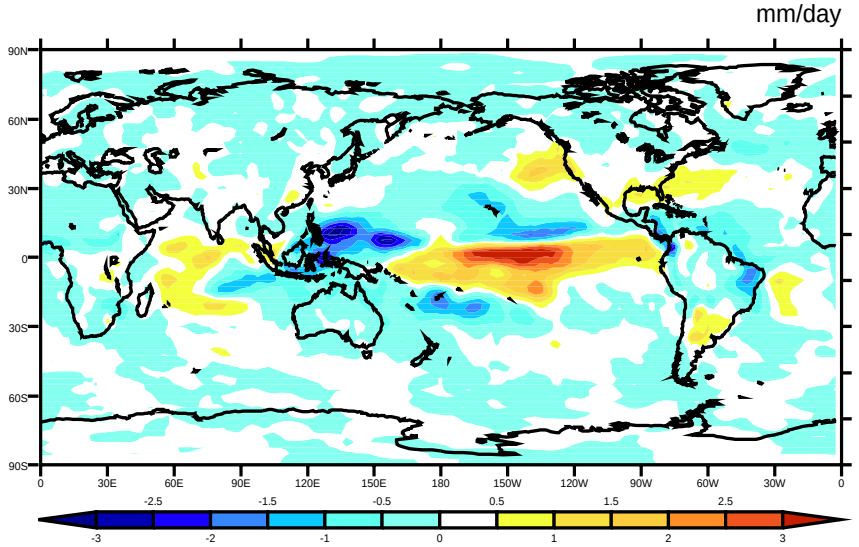

Figure 9

HadCM2. Control Run. Warm event anomalies for DJF

(a) TAS

(b) PSL

(c) PR

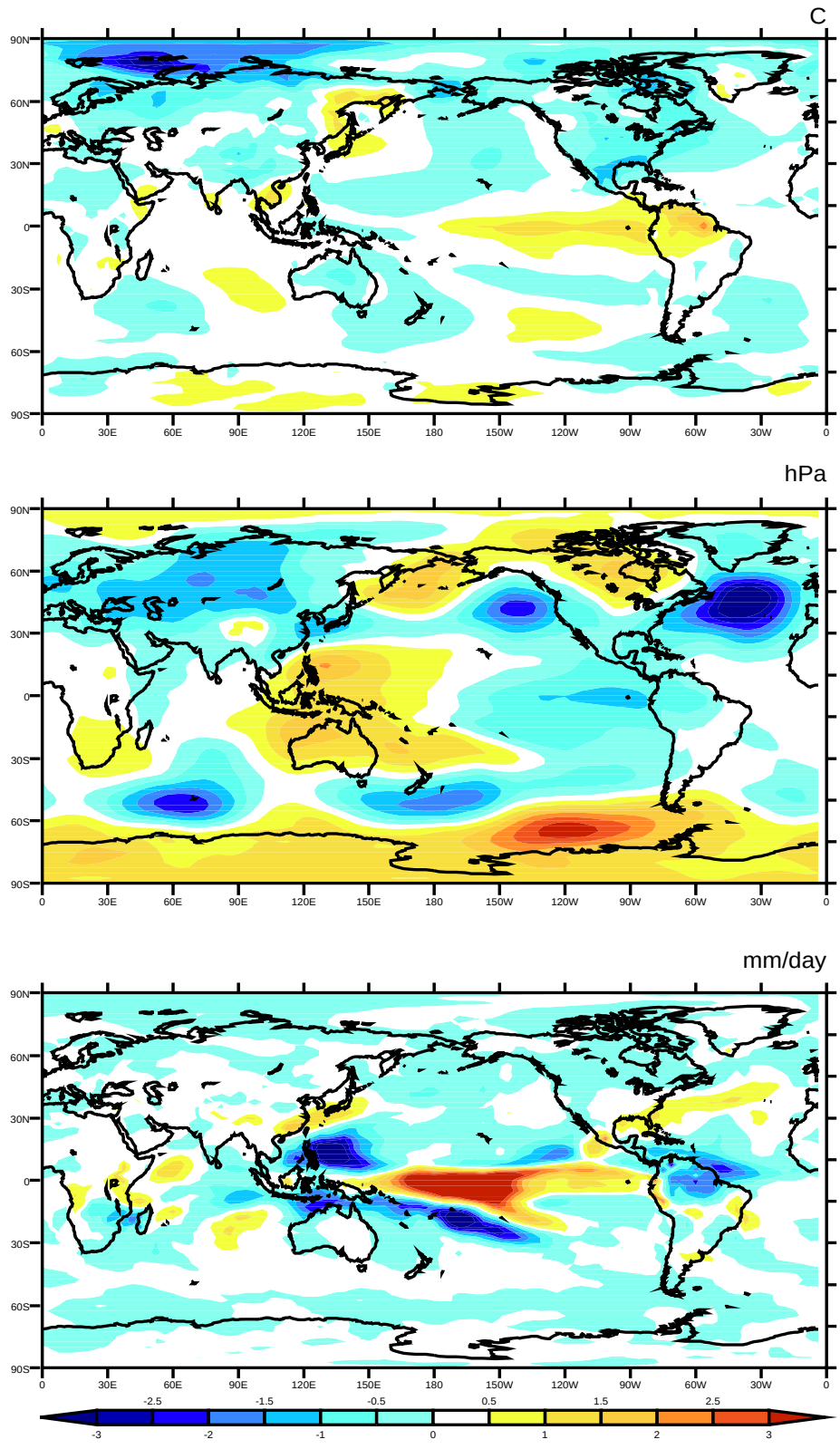

Figure 10

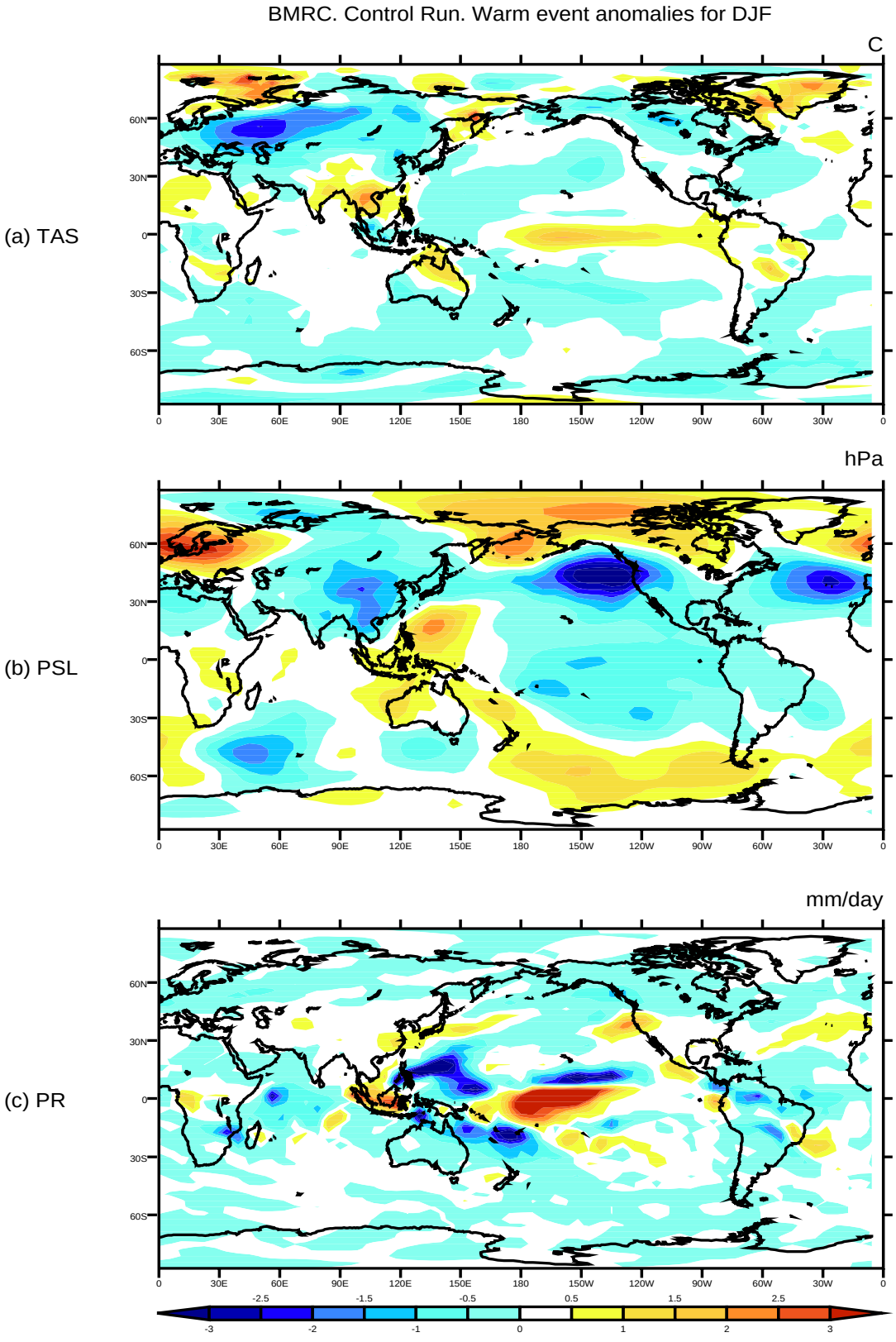
BMRC. Control Run. Warm event anomalies for DJF
C
(a) TAS
hPa
(b) PSL
mm/day
(c) PR
60N
30N
0
30S
60S
0
30E
60E
90E
120E
150E
180
150W
120W
90W
60W
30W
-2.5
-1.5
-0.5
0.5
1.5
2.5
-3
-2
-1
0
1
2
3

Figure 11

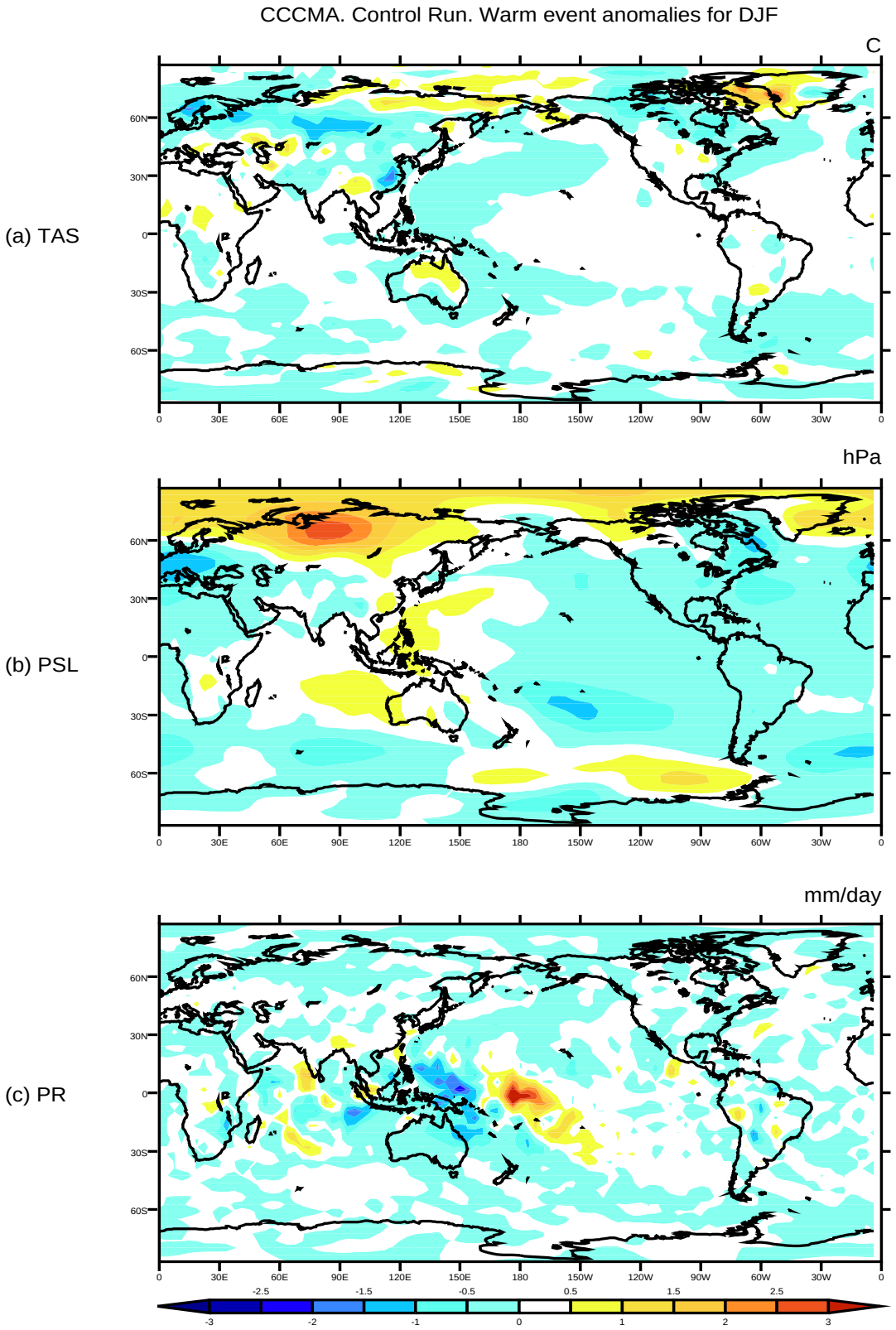
CCCMA. Control Run. Warm event anomalies for DJF
C
(a) TAS
60N
30N
0
30S
60S
0
30E
60E
90E
120E
150E
180
150W
120W
90W
60W
30W
0
hPa
(b) PSL
mm/day
(c) PR
-2.5
-1.5
-0.5
0.5
1.5
2.5
-3
-2
-1
0
1
2
3